Title

Aerobic exercise and scaffolds with hierarchical porosity synergistically promote functional recovery post volumetric muscle loss

Permalink

https://escholarship.org/uc/item/0492v004

Authors

Endo, Yori
Samandari, Mohamadmahdi
Karvar, Mehran
et al.

Publication Date

2023-05-01

DOI

10.1016/j.biomaterials.2023.122058

Peer reviewed

Aerobic exercise and scaffolds with hierarchical porosity synergistically promote functional recovery post volumetric muscle loss

Yori Endo[1,‡], Mohamadmahdi Samandari[2,‡], Mehran Karvar[1,‡], Azadeh Mostafavi[3], Jacob Quint[2], Chiara Rinoldi[4], Iman K. Yazdi[5], Wojciech Swieszkowski[4], Joshua Mauney[6], Shailesh Agarwal[1], Ali Tamayol[2,3]*, Indranil Sinha[1,*]

[1]Division of Plastic Surgery, Brigham and Women's Hospital, Harvard Medical School, Boston, MA 02115, USA

[2]Department of Biomedical Engineering, University of Connecticut, Farmington, CT 06269, USA

[3]Department of Mechanical and Materials Engineering, University of Nebraska-Lincoln, Lincoln, NE 68588, USA

[4]Materials Design Division, Faculty of Materials Science and Engineering, Warsaw University of Technology. Warsaw 02-507, Poland

[5]Division of Engineering in Medicine, Brigham and Women's Hospital, Harvard Medical School, Boston, MA 02115, USA

[6]Departments of Urology and Biomedical Engineering, University of California, Irvine, Irvine, CA 92868, USA

[‡]: Y. Endo, M. Samadari, and M. Karvar contributed equally to the manuscript.

*Corresponding authors: A. Tamayol: atamayol@uchc.edu; I. Sinha: isinha@bwh.harvard.edu

Abstract

Volumetric muscle loss (VML), a composite defect of skeletal muscle, heals by scarring and minimal muscle regeneration, leading to permanent disability. Current surgical and physical therapies are inadequate and therefore regenerative therapy is needed for effect treatment of VML. The present study showed that a significant loss of muscle mass and function was accompanied by a down-regulation of insulin-like growth factor 1 (IGF-1) responsible for muscle maintenance and regeneration. Treatment of myoblasts with 10 ng/mL of IGF-1 promoted their proliferation and differentiation *in vitro*. In light of this, a colloidal scaffold with hierarchical porosity that sustains efficacious levels of recombinant IGF-1 was engineered. The foam-like scaffold was directly crosslinked onto remnant muscle without the need for suturing. The scaffold demonstrated a compressive modulus of 9 ± 2 kPa and an adhesion strength of 11 ± 3 kPa. Post implantation, the foam-like scaffolds carrying IGF-1 significantly improved functional recovery as measured by muscle force production. Histological analysis confirmed regeneration of new muscle in the engineered scaffolds. In addition, the scaffolds significantly reduced fibrosis and increased the expression of neuromuscular junctions in the newly regenerated tissue. Exercise therapy when combined with the foam-like scaffolds augmented the treatment outcome in a synergistic fashion.

In situ 3D printing of IGF-1-releasing porous muscle scaffold onto extensive muscle injuries resulted in robust tissue ingrowth and muscle repair.

1   Introduction

Skeletal muscle enables movement, protects internal organs from impact, and participates in vital actions such as chewing and maintaining temperature homeostasis [1-3]. Skeletal muscle possesses a high regenerative capacity to heal minor injuries, which is necessary to maintain its mass and strength [4,5]. The natural regeneration of skeletal muscle happens through a cascade of physiological events resulting in activation of quiescent satellite cells [6-8]. Following injury, activated muscle stem cells proliferate, differentiate into myocytes, and then either fuse together to form new multinucleated muscle fibers or fuse to existing myotubes and promote hypertrophy [9]. However, volumetric muscle loss (VML), which are composite skeletal muscle injuries, overwhelms the regenerative potential of muscle. These injuries, especially when they comprise 20% or more of the muscle belly, heal with poor regeneration and extensive fibrosis, resulting in chronic functional deficits [10,11]. Following VML, downregulation of myogenic factors and upregulation of profibrotic factors all limit strength and functional recovery, especially in the absence of scaffold placement [12,13].

Therapeutic options for VML injury remain limited. Currently, free tissue transfer of functional muscle is the standard treatment for substantial VML injuries [14-16]. However, this approach leads to limited functional recovery and donor site morbidity [16]. Targeted physical therapy may also improve recovery following VML but its benefit is limited [17]. Tissue engineering offers an alternative strategy to VML treatment. An engineered muscle graft for promoting skeletal muscle regeneration can be constructed by the integration of myogenic factors and cells into scaffolding materials that mimic the native extracellular matrix [1,18,19]. A promising method to fabricate such scaffolds as a replacement for the lost tissue is 3D (bio)printing [1,20,21]. 3D (bio)printing is used as an additive manufacturing strategy through which bioinks are deposited in a controlled manner for the biofabrication of tissue-like constructs [22]. 3D (bio)printing can fabricate complex muscle grafts with clinically relevant sizes [23]. However, this strategy suffers from a number of challenges, namely the need for scanning modalities to reproduce the defect morphology, computer-aided design and manufacturing (CAD/CAM) tools and expertise, and a properly isolated environment to prevent potential infection [24,25]. These standard technologies and requirements result in delayed implantation, limited tissue integration due to low tissue adhesion, and challenges for conformation into curved irregular defects [24,25]. One strategy that can overcome some of these limitations is the direct printing of scaffolds onto the patient's body, otherwise

known as *in vivo* or *in situ printing* [25]. *In situ printing* can be performed using a computer-controlled system depositing a bioink directly into a defect [26]. However, this approach still requires scanning and CAD/CAM implementation, along with sophisticated robotic systems.

To address the current issues regarding use of scaffolds as a therapeutic option for treatment of VML, we have developed handheld (bio)printers for *in situ printing* of scaffolds for skin [24], bone [27], and muscle [28,29] regeneration. The *in situ printing* using this strategy is rapid and actively controlled by the surgeon during the operation. This eliminates the requirement of CAD/CAM systems and scaffolds can be conformed to irregular defects with curved surfaces. Furthermore, the *in situ* crosslinking of bioink upon its deposition generally enhances its tissue adhesion and therefore graft integration. However, functional recovery of injured muscle treated with this technique was previously shown to be limited by poor tissue ingrowth and limited induction of muscle regeneration within the scaffold itself [29]. These results support the delivery strategy, but highlight the need for bioinks with specific properties to support both biofabrication and tissue regeneration. Ideally, 3D scaffolds should recapitulate the biological and physical properties of the extracellular matrix to assist with muscle regeneration, support cellular infiltration, proliferation, and differentiation, and promote distribution of nutrients and oxygen [30-32]. While significant effort has been put into the engineering of various cell-permissive scaffolds, the dense polymeric network of printable bioinks usually limits normal cellular behavior and affects their migration, proliferation, and maturation. This in turn leads to poor myogenesis, vascularization, and innervation [33-35]. Limited diffusion of nutrients into these scaffolds further impedes cellular activity, especially within larger constructs that are required for VML [36,37]. A possible solution for this is to incorporate hollow channels within the scaffold through multimaterial bioprinting [38,39]. However, this strategy is complex and can be challenging to implement with *in situ* printing, as such porosity negatively impacts mechanical properties, fidelity, and structural stability of the printed construct.

The engineered scaffold can be supplemented with myogenic factors to enhance the regenerative response of injured muscle. Various biochemical factors, mainly provided by immune cells and platelets, have been reported to contribute to different stages of muscle regeneration [8,40]. One of the most notable myogenic factors in muscle regeneration is insulin-like growth factor-1 (IGF-1), which is known to promote satellite cell proliferation and differentiation, as well as immune modulation [41]. However, exogenous IGF-1 therapies have clinically failed due to toxicity

and adverse effects of systemic delivery or difficulty in maintaining therapeutic IGF-1 concentrations at the injury site after bolus injections [42,43]. Therefore, a delivery system that allows localized, sustained release of IGF-1 within injured skeletal muscle is required for attaining adequate myogenic effect of the growth factor [44].

Here, we develop a simple and clinically implementable strategy to address the above-mentioned requirements for both the biomaterial ink as well as biofabrication and implantation approach. We have engineered frothy scaffolds with multi-scale porosity to enhance cell permissibility, carrying IGF-1-loaded microparticles to enable its sustained release for enhanced myogenesis. An *in situ* printing strategy was utilized to deliver the scaffold directly into muscle defects of a murine VML model. This scaffold was designed to adhere to the tissue directly and offer a temporary 3D myogenic microenvironment for cellular infiltration, proliferation, and differentiation toward the restoration of muscle structure and function. Lastly, as regimented exercise may promote functional recovery as well [45], we demonstrated that exercise therapy combined with the acellular, foam scaffold offers the most complete recovery following acute VML. Given the acellular nature of the scaffolds, it holds promise for rapid translation into clinical use for patients with VML injuries.

2   Results

Following VML injury, loss of cellular, structural, and chemical components necessary for healing limits effective muscle regeneration and leads to permanent loss of function [12,13]. Here, a murine model of VML of the posterior compartment of the leg was utilized as previously described [17]. Evaluation of gross images of injured muscle without any intervention confirmed minimal restoration of lost muscle volume eight weeks following VML injury (**Figure 1A**), indicating poor muscle regeneration and recovery. Furthermore, *in vivo* ankle torque measurements demonstrated approximately a 50% reduction in muscle force production immediately after VML injury. Ankle torque remained approximately 30% lower than muscle that underwent a sham operation eight weeks after VML (**Figure 1B**). An enzyme-linked immunosorbent assay (ELISA) demonstrated significantly lower levels of IGF-1 ($p = 0.002$) within the remnant skeletal muscle tissue at 3.7 ± 2.3 ng/g in the VML injured group, as compared to 9.2 ± 2.5 ng/g (mean $\pm$ SD) in uninjured animals two weeks after VML injury (**Figure 1C**). These results suggest that the loss of extracellular matrix (ECM) and diminished local level of myogenic factors associated with VML

may partially cause a reduced regenerative capacity within the remnant tissue and promote a shift to repair mechanisms of healing, such as fibrosis. Therefore, regenerative therapies may need to include both scaffolds that support tissue ingrowth and sustained release of myogenic factors, specifically IGF-1, to be efficacious.

To achieve this goal, we developed a strategy based on the *in situ* printing of highly porous GelMA-based scaffolds that could control the release of IGF-1 (**Figure 1D**). *In situ* printing as the delivery method of this noble scaffold was elected due to its simplicity and high potential for translation into a clinical treatment of VML. Due to favorable cellular adhesion, biodegradability, and tunability of physical and chemical properties [46,47], GelMA was selected as the primary biomaterial forming the bioink for *in situ* printing. However, the dense polymeric network of the GelMA hydrogel limited cellular infiltration and scaffold integration in our previous studies [29]. To enhance the cellular permissibility of the scaffold, a simple foaming method, inspired by whipped cream production for pastries, was considered to introduce mesoscale pores into the GelMA structure. On the other hand, GelMA, which is mainly synthesized with type A gelatin, is positively charged at neutral pH [48] and consequently unable to bind to electropositive IGF-1 [49]. Therefore, negatively charged gelatin type B [48] microparticles were selected to be incorporated into the structure to serve as a linkage element.

Figure 1D illustrates a schematic overview of the designed concept and process for the treatment of VML in this study. Initially, gelatin microparticles are loaded with IGF-1 and encapsulated into a GelMA precursor. Subsequently, the solution is stirred at high speed to foam the biocomposite and form the final bioink. The bioink is then directly printed onto the VML defect using a handheld printer. *In situ* crosslinking stabilizes the printed filaments and leads to their adhesion to remnant tissue [29]. The hierarchical pores were expected to enhance the cellular permissibility and sustain the release of IGF-1, thus promoting rapid proliferation and differentiation of infiltrating cells to regenerate muscle and restore its lost function.
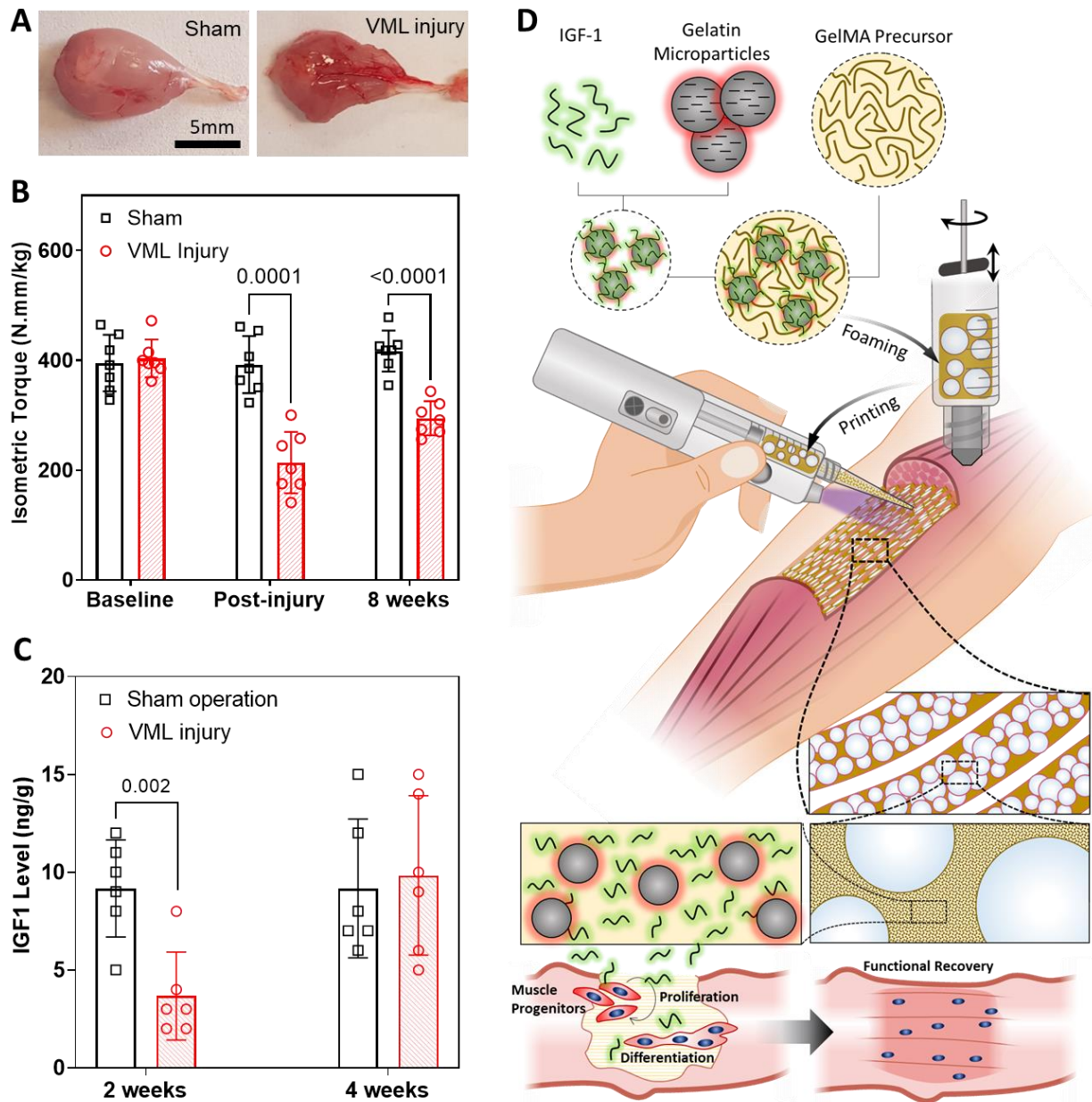
Figure 1. **Murine VML model and the proposed strategy for its treatment**. (A) Gross images of the extracted muscles 8 weeks post-surgery. Lack of regeneration and smaller volume of the muscle in the VML injury group compared to the sham group confirmed the applicability of the VML injury model. (B) Force generation capability of the muscle post VML injury. A significant reduction was detected in the measured isometric torque immediately after defect induction, as well as eight weeks post-surgery, demonstrating a deficit of the muscle post VML. (C) Assessment of IGF-1 level in remnant muscle post VML. A significant reduction in the concentration of IGF-1 was observed two weeks post VML injury. Considering the requirement of IGF-1 in natural muscle regeneration, a reduced level of this growth factor can be considered a major contributor in impaired regeneration post VML. (D) The proposed strategy for the treatment of VML. Negatively charged gelatin nanoparticles are synthesized to link positively charged IGF-1 into a positive GelMA structure. The precursor is then foamed and directly printed into the muscle defect

using an *in situ printing* method with a custom handheld printer. The printed scaffolds adhere to the remnant tissue and possess a mesoporous structure to facilitate cell infiltration. The release of IGF-1 then is expected to enhance the activity of infiltrated cells toward muscle regeneration and its functional recovery.

2.1 The effect of IGF-1 on muscle progenitors

To assess a suitable range of IGF-1 concentrations to enhance cell proliferation and myogenesis, C2C12 myoblast cells were treated with different IGF-1 concentrations *in vitro* (**Figure 2**). The results demonstrated that 10 ng/ml of IGF-1, a concentration close to the physiological concentrations in muscle (**Figure 1C**) had a significant effect (p = 0.0004 and p < 0.0001, respectively, on day 3 and day 7 of culture) on proliferation of myoblasts measured by the metabolic activity (**Figure 2A**). F-actin/nuclei staining of cultures showed a better alignment and organization in cultures treated with 10 ng/ml of IGF-1 (**Figure 2B**). This may reflect a higher proliferation rate and enhanced cellular communication between proliferating cells in the presence of IGF-1 [39].

Gene expression was assessed to further evaluate the effect of IGF-1 on myogenic differentiation. Two myogenic markers (α-actinin and MRF4), an ECM component (type I collagen), and a cell adhesion marker (β1-integrin) were selected for assessment of myogenic behavior in differentiating muscle cells [46,50] (**Figure 2C-F**). The results demonstrated that supplementation of the cells with IGF-1 significantly promoted myogenic differentiation (**Figure 2C, D**). α-actinin, a molecule that contributes to force generation was expressed around 16 folds higher when cells were exposed to IGF-1 at physiological concentrations (10 ng/ml, **Figure 2C**). Similarly, the expression of MRF4, a late myogenic marker [46], was doubled in cultures treated with 10 ng/ml IGF-1, as compared to vehicle control, by day three in culture (**Figure 2D**). The enhanced expression of myogenic markers (normalized to GAPDH housekeeping gene) could be a direct effect of IGF-1 exposure, as well as an indirect effect of cellular proliferation. It has been previously reported that IGF-1 can improve the differentiation and maturation both directly and through enhanced cellular communications upon increased proliferation [8,41].

These results further suggest that not only the myogenic differentiation, but also ECM deposition and cell-cell/cell-ECM adhesion were enhanced with IGF-1 supplementation at both 1 ng/ml and 10 ng/ml concentrations, but more significantly at higher concentrations comparable to

the physiological level in healthy muscle (**Figure 2E, F**). As such, the loss of IGF-1 seen following VML injury may impair skeletal muscle regeneration and differentiation within the area of VML.
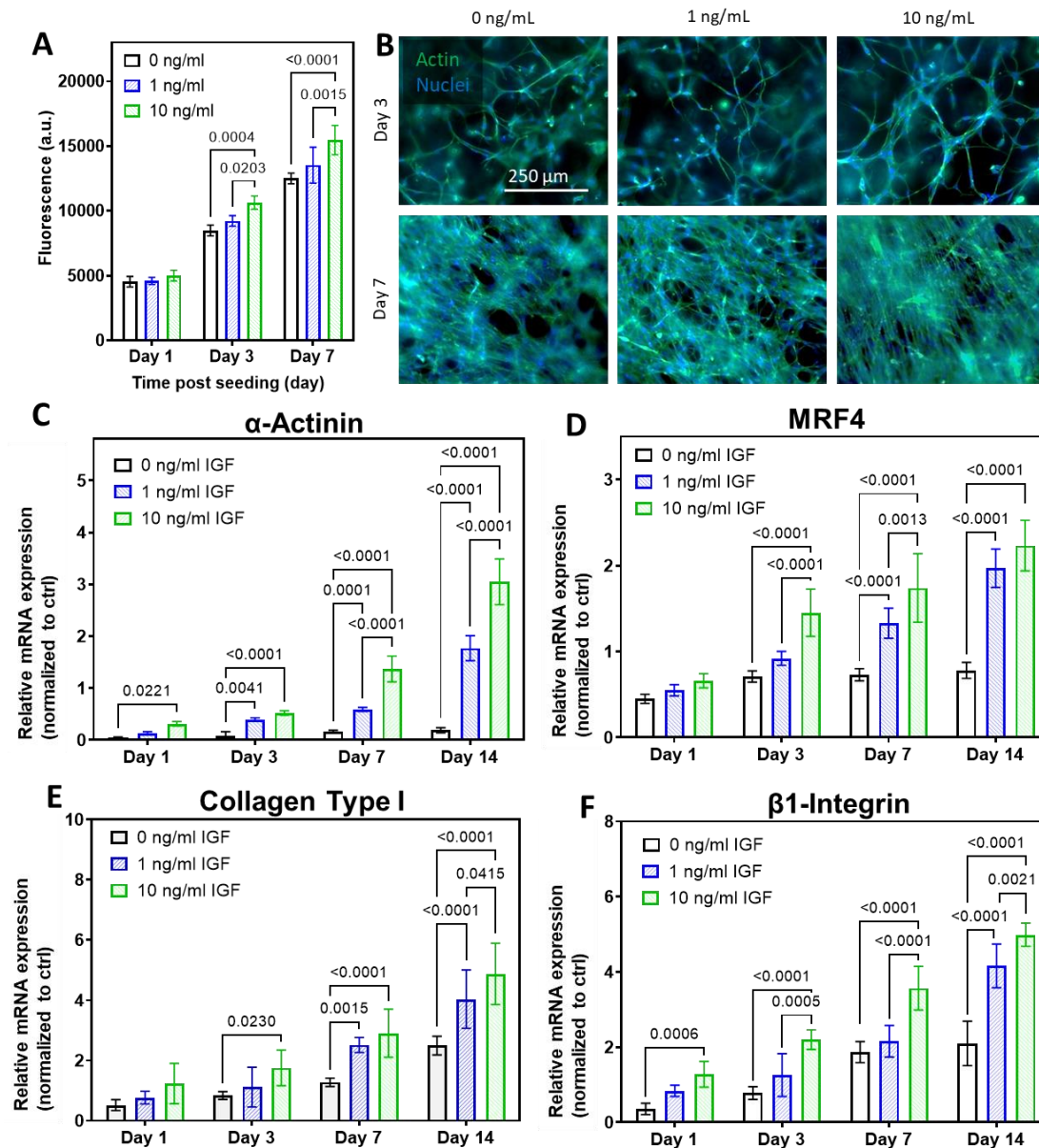

Figure 2. *In vitro* **effect of IGF-1 on C2C12 muscle progenitors.** (A) Metabolic activity of myoblasts, exposed to different levels of IGF-1, over one week in culture condition. IGF-1 at a physiological concentration (10 ng/ml) significantly enhanced metabolic activity suggesting cellular proliferation. (B) F-actin/DAPI staining of cells exposed to different IGF-1 levels on days 3 and 7 of culture. Enhanced proliferation and consequent alignment can be observed in cells exposed to 10 ng/ml IGF on day 7. (C-F) Gene expression analysis of the cellular behavior during differentiation. The expression of two myogenic markers α-actinin (C) and MRF4 (D) demonstrated a significant improvement in cellular differentiation. The expression of Collagen I (E), an ECM protein, and β1-integrin (F), a cell adhesion molecule, were also significantly increased during differentiation.

2.2 Development and characterization of IGF-1 eluting scaffolds with multiscale porosity

After determining a suitable range of IGF-1 concentrations for enhancing myogenesis, a scaffold system with hierarchical pores that is permissive of cellular infiltration / activity and controlled IGF-1 local delivery was engineered [30]. **Figure 3A** demonstrates the microscopic structure of the scaffold. Mesoscale pores, with an average diameter of around 80 ± 4 µm was incorporated into the inherently porous GelMA hydrogel using a foaming approach (**Figure 3B**). A handheld high-speed stirrer (15000 RPM) was used to introduce microbubbles inside a 15% GelMA solution to generate a colloidal bioink (**Figure 3Ai**). Given the hydrophilicity of the hydrogel scaffold and differential densities of air and hydrogel, the bubbles quickly disrupt the thin membrane between them (**Figure 3Aii**; white arrowheads are pointing to the ruptured thin membrane), and are released from the scaffold when submerged it into an aqueous environment, generating an interconnected mesoporous scaffold. These large pores are also connected through microscale hydrogel pores inherent to GelMA (average size ≈ 6 µm) in other regions (**Figure 3Aiii**). These data together demonstrate the capability of this simple but robust process for the fabrication of scaffolds with hierarchically interconnected pores. Quantification of different pore sizes is shown in **Figure 3B**.

Retained IGF-1 was expected to support proliferation, differentiation, and function of resident satellite cells to promote skeletal muscle regeneration and recovery. To achieve an initial burst release, part of the IGF-1 was freely mixed with the GelMA precursor. To retain part of IGF-1 in the above-mentioned scaffold to interact with infiltrating cells, gelatin microparticles were synthesized, electrostatically loaded with IGF-1, and supplemented into the GelMA precursor. **Figure 3C** shows the synthesized gelatin microparticles, with an average size of ≈ 4 µm before rehydration and loading (**Figure 3D**). The microparticles swell during loading. The particles were synthesized to be large enough to be constrained and encapsulated by the photo-crosslinked GelMA hydrogel network. Furthermore, the negatively charged gelatin type B microparticles could electrostatically interact with positively charged GelMA scaffold synthesized from type A gelatin and generate a higher level of affinity. Like the GelMA hydrogel, the gelatin microparticles are enzymatically degradable, but their relatively large size after rehydration inhibits their ability to escape beyond the local scaffold inherent pores or injury environment and are too large for systemic exposure [51]. Yellow arrowheads in **Figure 3Aiii** show the adhered and entrapped gelatin microparticles within the GelMA network. In an *in vitro* release, the IGF-1 loaded particles

encapsulated in the GelMA network enabled partial retentionof IGF-1 within the scaffold, slowing the overall release compared to the foam group without microparticles (**Figure 3E**). The microstructure of the foam increased the diffusion of IGF-1 compared to bulk GelMA scaffolds resulting in a higher total release. Due to the electrostatic difference of positive IGF-1 and the negative gelatin microparticles, the burst release of IGF-1 from the scaffold was diminished in the foam and particles group compared to the foam alone group, and the foam and particles group enabled the release of the growth factor at physiologically relevant concentrations (>1ng/ml per day) for multiple days (**Figure 3E**).

The mechanical properties of the scaffold were further measured to evaluate the effect of microporosity and incorporated particles on the scaffold's stiffness (**Figure 3F**), and the values with adhesion to native muscle tissue were compared (**Figure 3G**). Compression tests demonstrated that the Young's modulus of the GelMA hydrogel (15% w/v) decreased significantly ($p < 0.0001$) from 76 ± 10 kPa for bulk GelMA to 8 ± 2 kPa after foaming. The addition of gelatin microparticles did not significantly affect these results (**Figure 3F**). Interestingly, these results demonstrate that the stiffness of the foam resembles the bulk properties of native skeletal muscle (compressive modulus around 12 kPa [52]), while the stiffness of GelMA is similar to that of native muscle fibers (compressive modulus around 50 kPa for fast and 100 kPa for slow twitch fibers [53]).

To evaluate the adhesion of the engineered biomaterials on muscle upon *in situ* printing, a shear test was performed as shown schematically in **Figure 3G**. The bioink was printed on muscle tissue glued to a glass slide, covered with a TMSPMA coated glass slide, and the hydrogel was then crosslinked *in situ*. The results show that *in situ* crosslinking of both GelMA and the foam promote adherence to muscle tissue (adhesion strength > 9 kPa). The adhesion strength was reduced from 16 ± 1 kPa for GelMA hydrogel to 9 ± 2 kPa for foam ($p < 0.002$). The less pronounced difference in adhesion strength of the foam and hydrogel in comparison to the difference in compressive moduli could be attributed to the significant deformability of the foam (**Figure S1**). Furthermore, incorporation of gelatin microparticles only slightly increased the adhesion strength of the foam and muscle to 11 ± 3 kPa.

Finally, the ability of the bioink to form filaments and maintain the multiscale porous structure upon deposition and crosslinking was evaluated. The printability of the foam was assessed through evaluation of the bioink status on the nozzle tip as previously described [54]. **Figure 3H** shows that the extruded foam from the nozzle tip had a smooth filament morphology, which

confirms the printability of this bioink [54]. Furthermore, the bright-field micrograph of a printed filament, shown in **Figure 3I**, shows the preserved mesoporous structure of the bioink after deposition, as well as a smooth and uniform filament size along the printing direction.
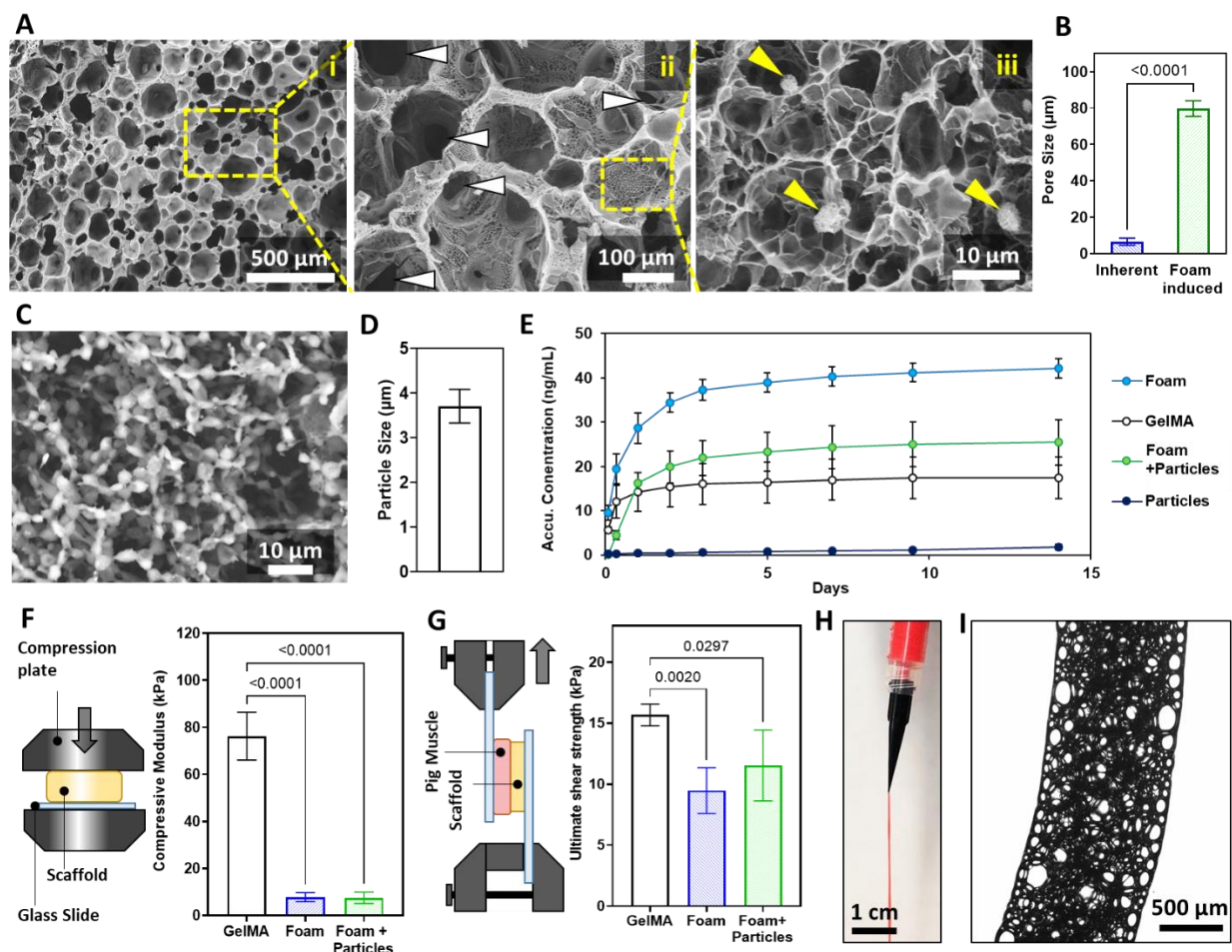

Figure 3. Development and characterization of the engineered bioink. (A) SEM micrographs demonstrated the multiscale porous structure of the foam bioink and incorporated gelatin microparticles into the structure. (i), (ii), and (iii) show pores in different scales ((i) indicates the foam-induced mesopores and (iii) indicates the inherent micropores). White arrowheads in (ii) show ruptured thin membranes between the bubbles, as a result of foam submersion in saline solution, forming an interconnected mesoporous structure. Yellow arrowheads indicate the adhered gelatin microparticles into the structure. (B) Quantitative assessment of different pore sizes in the engineered scaffold. (C) SEM image of gelatin microparticles after synthesis. (D) The size of gelatin microparticles measure from SEM micrographs using ImageJ software. (E) Release profile of IGF-1 growth factor from microparticles, foam, foam with microparticles, and solid GelMA. A majority of the IGF-1 release occurred in the first few days in the hydrogel groups due to the freely bound IGF-1. IGF-1 continued to be released from the scaffold over the 14-day period. The IGF-1 bound to the gelatin microparticles resulted in a slower release than the foam only group. The microparticles retained most of the loaded IGF-1. (F) Compression test for evaluating the mechanical properties of the scaffolds. The test setup is shown schematically on the left, while the results are graphed as compressive modulus on the right. A significant decrease was detected

upon foaming, while the incorporation of microparticles did not significantly affect the results. (G) Evaluation of scaffold adhesion capability to the tissue. A shear test (left schematic) was used to measure the adhesion of the printed scaffold to the muscle and results were graphed as ultimate shear strength (right graph). While the adhesion significantly decreased through foaming, all of the scaffolds demonstrated strong adhesion to the tissue as a result of *in situ* crosslinking. (H) A smooth long filament extruded from the nozzle tip demonstrated a high level of foam bioink printability. (I) Bright-field micrograph of a printed filament showing the preserved mesoporous structure of the scaffold after printing.

2.3 In situ printing of the engineered scaffolds for the treatment of VML injury

A murine model of posterior compartment VML injury of the leg, as described in the first section of the results, was implemented here to evaluate the efficacy of foam scaffold treatment of VML (**Figure 4**). Four different groups were included in the study to evaluate the efficacy of the *in vivo* printed IGF-1-eluting scaffold with multiscale porosity on muscle regeneration: (i) a sham operation with no muscle injury, (ii) VML injury without any treatment (VML Untreated), (iii) VML injury followed by *in situ* printing of foam scaffold (VML + Foam), and (iv) VML injury followed by *in situ* printing of IGF-1-eluting foam scaffold (VML + Foam + IGF). **Figure 4A** schematically shows the workflow of this animal study. On day 0, VML injury was induced in the gastrocnemius (GA) muscle of mice bilaterally, followed by treatment of the injuries according to the above-mentioned groups. For this procedure, the skin was opened (**Figure 4Bi**), around 30% of the GA muscle mass was removed with a 4 mm biopsy punch (**Figure 4Bii, iii**), and the engineered bioink was directly printed into the defect and simultaneously crosslinked *in situ* (**Figure 4Biv, v**). For *in situ* printing, our custom handheld printer [24,28] with an integrated photocrosslinking mechanism was utilized (**Figure 4C**). In all experiments, the foam adhered securely to the remnant muscle tissue despite the wet microenvironment of the wound (**Figure 4Bv**), preventing scaffold movement during skin closure following the procedure. Eight weeks following the surgery, functional recovery of the hindlimbs was assessed through *in vivo* torque measurement, followed by *in situ* twitch and tetanus force measurement of GA muscle, and finally, the muscle tissues were harvested for future histological analysis.

Gross representative images of the harvested muscle eight weeks post-surgery demonstrate the restored muscle volume in different groups (**Figure 4D**). As previously shown, the regeneration in the VML Untreated group was minimal, while both VML + Foam and VML + Foam + IGF groups demonstrated a high level of regeneration. The quantitative measurements of muscle strength agree with these gross observations (**Figure 4E, F**). The results of torque

measurements, which evaluated ankle plantar flexion, (**Figure 4E**) demonstrated a significant (p = 0.0158) recovery in the VML + Foam + IGF group (348.5 ± 26.5 Nmm/Kg) compared to the untreated injuries (286.3 ± 24.2 Nmm/Kg). Furthermore, the average tetanus strength of GA was significantly higher with (p = 0.0120) VMLs treated with *in situ* printing of Foam + IGF (67.6 ± 19.8 mN/mm^2) compared to the VML Untreated group (36.9 ± 10.5 mN/mm^2).
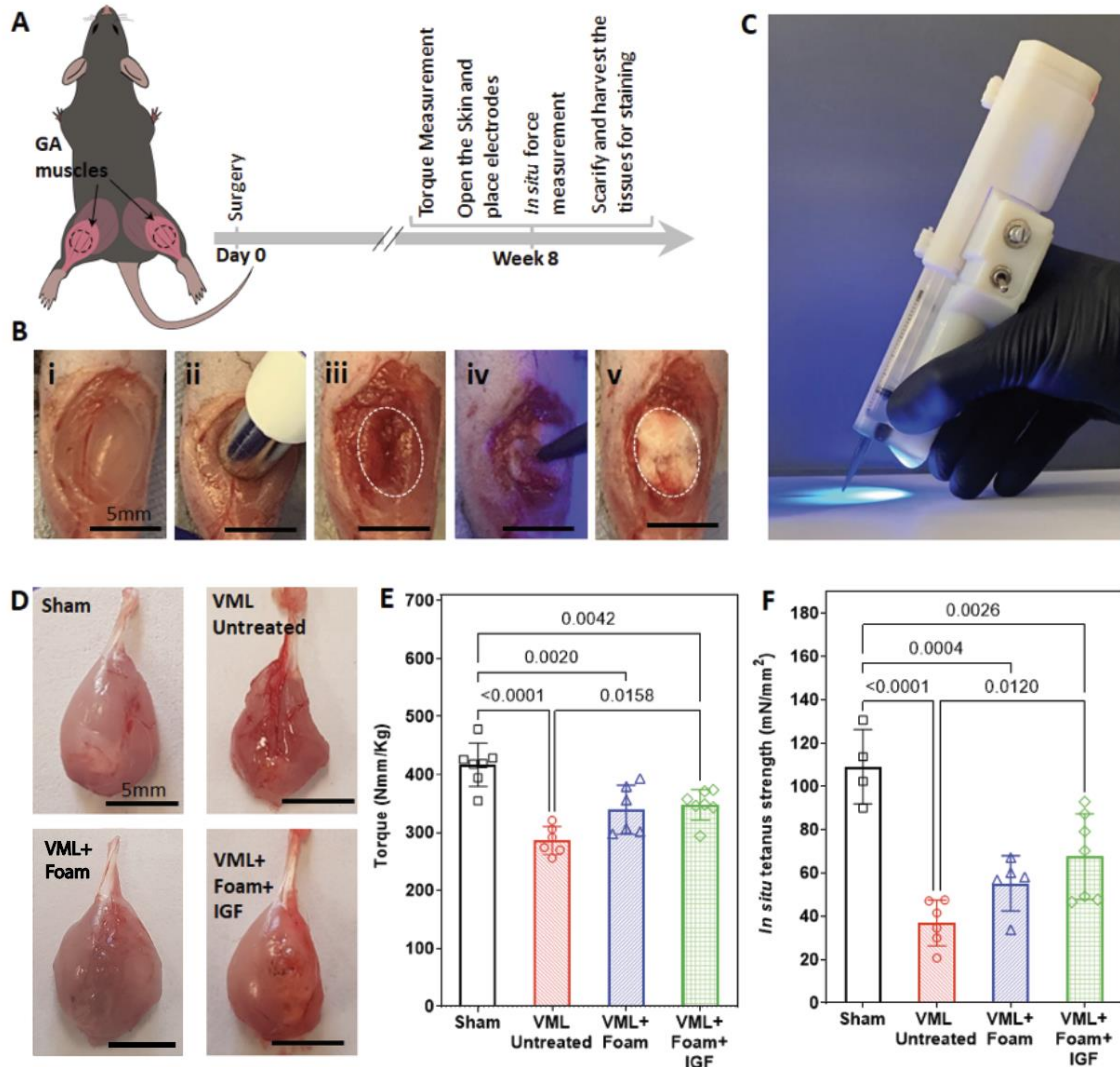

Figure 4. Application of *in situ printing* of engineered bioink for murine VML treatment and macroscopic evaluation of its effectiveness. (A) The workflow of animal studies is depicted. On day 0, surgeries were performed through induction of VML in GA muscle of both mice legs, and treatments were applied as shown in (B). After 8 weeks, the functional recovery of the legs strength was measured using torque measurement, followed by direct *in situ* measurement of GA muscle force generation. The animals were then sacrificed and tissues were harvested for histologic

analysis. (B) The VML induction and treatment procedure. After opening the skin, the GA muscle was exposed (i) and a 4 mm biopsy punch was implemented (ii) to remove ~30% of the muscle mass (iii). Then, the engineered bioink was directly printed in a VML defect and crosslinked *in situ* (iv, v). (C) The custom handheld printer with an integrated photocrosslinking mechanism was used for this study. (D) Gross representative pictures of harvested GA muscle demonstrating the restored volume of the muscle eight weeks post- surgery as a result of *in situ printing* of the engineered scaffold. (E) Assessment of functional recovery of the leg strength using torque measurements. Significant functional recovery was detected in VML + Foam + IGF group compared to untreated muscles. (F) Evaluation of GA muscle recovery after eight weeks of VML induction through *in situ* tetanus force measurements. A statistically significant recovery was detected in muscles treated with VML + Foam + IGF compared to untreated muscles.

Next, histological analysis was performed to assess muscle regeneration from a microscopic perspective (**Figure 5**). Masson Trichrome (MT) staining of muscle cross sections showed that while extensive fibrosis was present in remnant muscles following untreated VML injuries, soft tissue reconstitution and decreased fibrosis were notable in both foam and foam supplemented with IGF-1 loaded microparticles treated VML injuries (**Figure 5A, B**). The regeneration of muscle fibers was further evaluated (**Figure 5C**) using triple-immunofluorescence staining of the basal lamina component (laminin), sarcomere myosin heavy chain that marks mature, remnant fibers (MF20), and embryonic myosin heavy chain that marks regenerating fibers (eMHC). The injury site of untreated VML showed limited signs of muscle regeneration, with few regenerating fibers poorly aligned to the remnant myofibers, in contrast to VML injuries treated with foam and IGF-, which demonstrated multiple regenerating fibers (**Figure 5C**). Finally, in order to assess the level of muscle maturation and functional capacity, triple-immunofluorescent staining for laminin, cell nuclei (DAPI), and acetylcholine receptor (AChR), a component of neuromuscular junctions (NMJs), was performed on the harvested muscle tissues (**Figure 5D**). While some innervation (shown by white arrows) was indicated by the presence of a few post-synaptic AChRs in both treatment groups, the VML + Foam + IGF group seems to have the greatest density of AChRs within the injured area.

Quantitative analysis of staining signals suggests further advantages of the proposed strategy for VML treatment (**Figure 5E-G**). Measurement of collagen deposition area (**Figure 5E**) demonstrated a significant reduction in the level of fibrosis in both VML + Foam (11 ± 3 %) and VML + Foam + IGF (10 ± 2%) groups compared to untreated injuries (20 ± 8%). Furthermore, while a statistically significant difference was not detected in the number of eMHC-expressing myofibers between different groups, a clear increasing trend toward the VML + Foam + IGF group

was observed, suggesting a relatively higher level of ongoing regeneration in this group (**Figure 5F**). Finally, AChRs (**Figure 5G**) demonstrated a significant (p = 0.011) increase in innervation when VML was treated with VML + Foam + IGF (3.0 ± 1.4) compared to VML Untreated (1.3 ± 1.0). There were no statistical differences in the AChR density between uninjured muscle the muscle injured with VML treated with *in situ* printing of IGF-1- eluting foam.
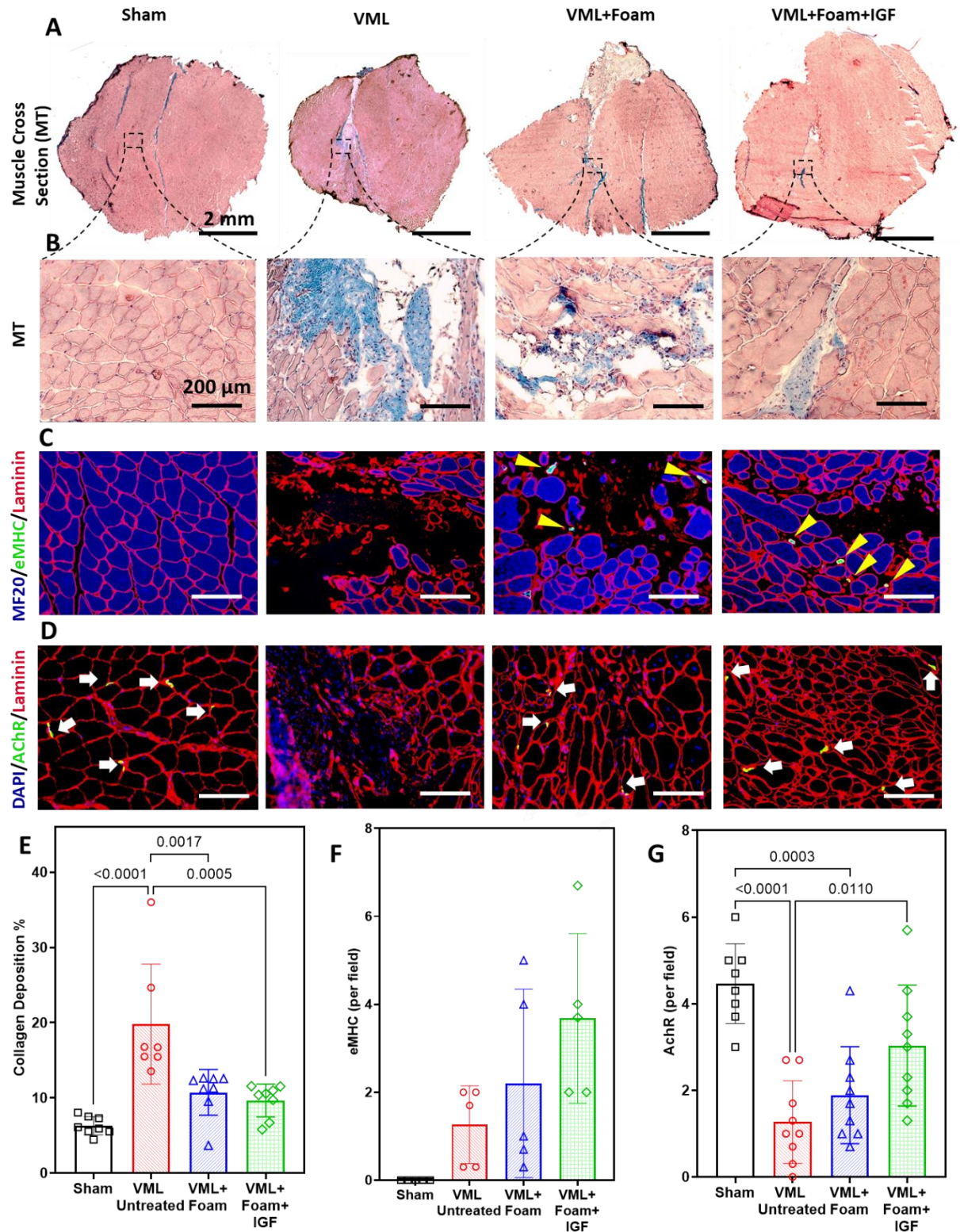
Figure 5. Microscopic evaluation of regeneration of VML injury treated with *in situ printing* of engineered scaffold 8 weeks post-surgery. (A) Cross sections of the muscle harvested from the mice and stained using the MT approach. The magnified images of the injury area are provided in (B). MT staining demonstrates a reduced level of fibrosis in both treatment groups compared to

VML Untreated group. (C) Triple-immunofluorescent staining for basal lamina (Laminin), sarcomere myosin heavy chain (MF20), and embryonic myosin heavy chain (eMHC). Denser and well-oriented muscle fibers with a higher amount of eMHC signal were observed in the injury area of the VML + Foam + IGF samples compared to other groups. Yellow arrowheads are indicating the eMHC stained cells. (D) Triple-immunofluorescent staining for Laminin, nuclei (DAPI), and acetylcholine receptor (AchR), a component of neuromuscular junctions. A higher level of AchR signal with nuclei positioned at the border of the fibers in the VML + Foam + IGF group suggests a high level of functional muscle regeneration. White arrows are pointing toward neuromuscular junctions stained with AchR. (E-G) Quantification of collagen deposition (E), eMHC signal (F), and AchR signal (G), corresponding to qualitative images shown in (A-D). Quantifications confirms lower fibrosis, indicated by lower collagen deposition, increased number of regenerating fibers stained with eMHC, and increased number of neuromuscular junctions stained with AchR, in the VML + Foam + IGF group compared to VML untreated group.

2.4 Synergistic effects of in situ printing and excursive therapy for VML treatment

In order to evaluate the effects of exercise on the different VML treatments, VML injuries were created bilaterally on the GA as previously described and were subsequently treated with either *in situ* printing of foam + IGF or no treatment. Sham groups, without VML injury, were used as negative controls. Following three days of recovery after sham operation or VML injury, all animals were acclimatized to running on a mouse treadmill for 3 days. The groups were then subjected to an 8-week-long exercise regimen comprised of running on *a* treadmill at 12 m/min for 40 minutes, three times weekly or no regimented exercise training program (**Figure 6A,B**). At the end of 8 weeks, the maximal distance of running was measured two days following the completion of the respective courses, and functional recovery of the injured GA muscle was tested through in situ measurement of tetanus force as described in the previous section.

Following the eight-week period of regimented exercise or no additional activity, mice with sham injury exhibited the greatest capacity for distance running distance (**Figure 6C**). Mice treated with foam and IGF following VML injury were able to run 30% further than mice with VML injury alone following regimented exercise training (p=0.02). *In situ* strength testing followed similar trends (**Figure 6D**). Mice which underwent sham injury exhibited the greatest strength in their gastrocnemius muscle. Exercise improved *in situ* gastrocnemius strength following VML treated with foam with IGF-1 by approximately 30% (p=0.04), but this improvement was absent in mice with VML injury alone. Additionally, VML treatment with IGF-1 and exercise improved *in situ* gastrocnemius strength by approximately 25% in comparison to VML injury following regimented exercise (p=0.04).
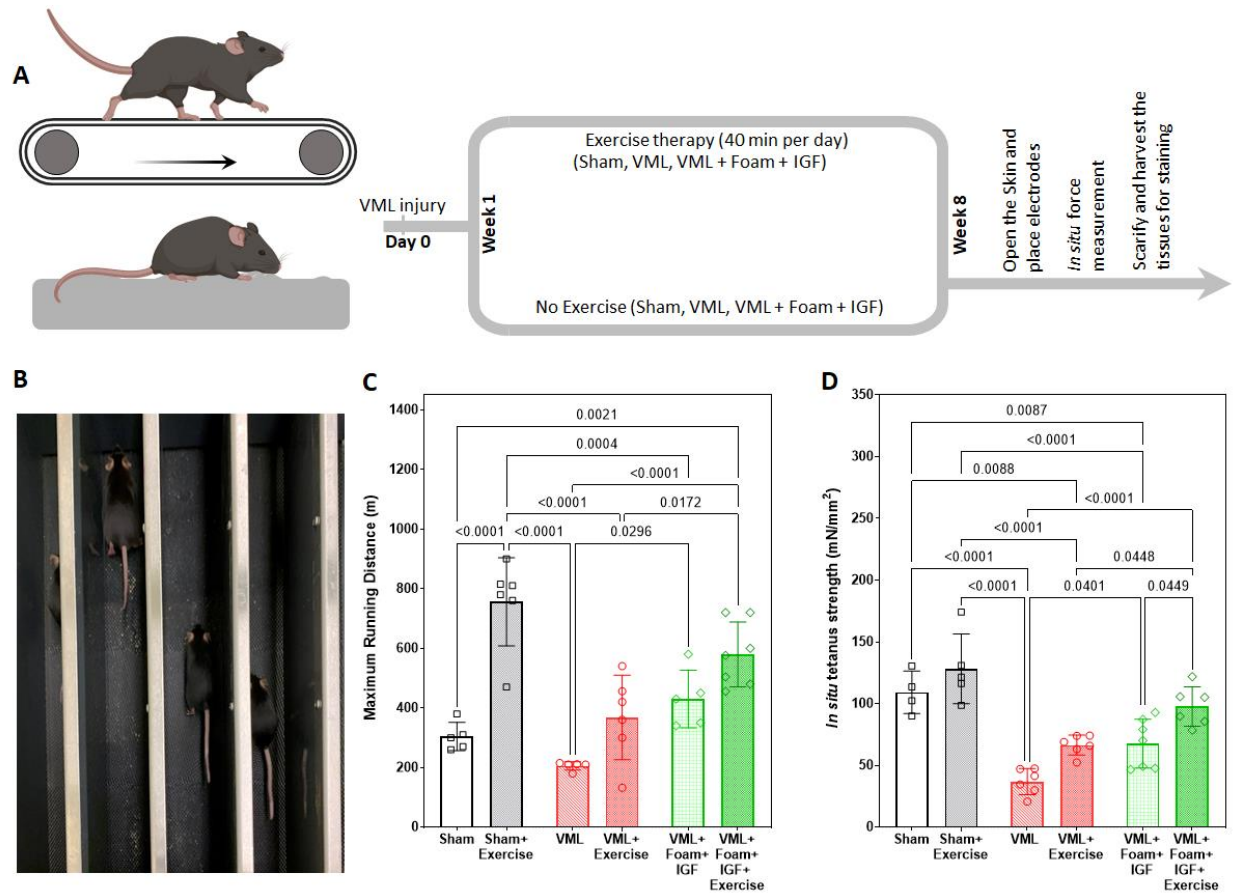
Figure 6. Combinational therapy through *in situ* printing of microengineered scaffolds and physical therapy. (A) A schematic of the 8-week-long exercise regimen. (B) The physical therapy was performed using a treadmill designed for the specific animal model. (C) Evaluation of the maximal distance of running. Exercise alone did not significantly improve the functional recovery of GA following VML injuries. VML + Foam + IGF + Exercise group demonstrated greater maximal running distance than VML and VML + exercise, indicating a synergistic effect of IGF foam with exercise on physiological recovery from VML. (D) Evaluation of GA functional recovery after eight weeks of VML induction through *in situ* tetanus force measurements. Exercise alone did not significantly improve the muscle strength, while significantly higher average muscle force was observed in the Foam + IGF as compared to the VML group. The VML+ Foam + IGF + Foam group showed significantly higher muscle strength than the VML. VML + exercise, VML + Foam + IGF groups, suggesting a synergetic effect of exercise on the Foam + IGF treatment following VML.

3   Discussion and Conclusions

While successful treatment of VML remains challenging, tissue engineering may offer a solution to improving patient recovery. In this study, we developed a simple, but effective strategy for VML treatment that combines regenerative therapy and regimented exercise. The strategy is based on the engineering of a bioink optimized for enhancing muscle regeneration and its delivery

using a highly translational and robust *in vivo* handheld printers. To improve the efficacy, the bioink addressed two important factors: (i) the requirement for a simple and clinically translatable preparation and application and (ii) the need for physiochemical properties permissive / promotive of myogenesis. GelMA was selected as the primary biomaterial constituting the bioink due to its biologically favorable structure providing cell-binding sites and biodegradable motifs, as well as its facile photocrosslinking [55]. However, standard GelMA, without any modification, suffers from important drawbacks: while very low concentrations of GelMA allow cellular migration within the 3D structure, the biofabrication and implantation of constructs made with low GelMA concentration are extremely challenging if not impossible [1]. Furthermore, such scaffolds degrade quickly in the harsh injury environment, limiting the efficacy of the scaffold for regeneration. Alternatively, high concentrations of GelMA can be implemented, but this significantly reduces cellular activity within the scaffold [1]. Considering that satellite cells as well as immune cells and other cell types responsible for muscle regeneration need a 3D space supporting a high level of cellular activity and nutrient turnover, GelMA is reported to be inadequate for proper muscle regeneration and functional recovery [1]. To overcome this, we developed a modified version of GelMA through simple stirring to incorporate mesoscale porosity into its structure.

The mechanical stirring initially introduces air inside the GelMA solution, followed by shear-induced bubble splitting that forms microbubbles [56]. While the protein nature of the GelMA can act as a surfactant and stabilize the generated microbubbles [57], PVA is used in the formulation to further prevent bubble merging and enable the formation of a stable colloidal bioink. Upon crosslinking, a multiscale porous structure consisting of foam-induced mesopores and inherent GelMA micropores is generated. Due to the proximity of the bubbles in the colloidal solution, a very thin membrane is formed between the pores where the bubbles were contacting, making the structure susceptible to rupture and formation of interconnected mesoporous morphology. Upon submersion into an aqueous solution, the thin membranes break with a driving force to merge and release bubbles from the structure to reduce the interfacial and gravitational energy of the system. The interconnected porous structure through both mesoscale and microscale pores provides an ideal environment for cellular activity as well as nutrient transport [58,59].

Previous investigations have studied the effect of mesopores on tissue regeneration [60,61]. It has been shown that mesopores, in the order of tens to hundreds of micrometers, not only enhance progenitor cells infiltration and proliferation but also reduce adverse inflammatory responses when

compared to the bulk hydrogels [60-62]. This is mainly due to the facile infiltration of immune cells inside the scaffold, without the need for excess secretion of proteases and pro-inflammatory factors [60-62]. Furthermore, such structures allow controlling mechanical properties independent of cell permissibility, since the cellular activity inside such structures is independent from the structure biodegradation [60,61]. Considering the importance of infiltration, proliferation, and differentiation of satellite cells into the implanted scaffold, as well as proper immune system activity in the muscle regeneration [1], the application of mesoporous scaffolds for VML treatment is highly promising. However, such mesoporous scaffolds have been primarily fabricated through cryogelation or annealing of microgel building blocks [60-62]. Unfortunately, such strategies are highly complex and time consuming, which makes them inadequate for translational applications and particularly *in situ* bioprinting. Here, we developed a simple and highly translational foaming approach which can induce mesoporosities while enabling *in situ* bioprinting. When combined with controlled release of IGF-1, which has been shown to enhance proliferation and differentiation of satellite cells [8,41] while modulating immune system [8], the mesoporous scaffolds proposed in this study significantly enhanced VML healing and functional recovery.

The multiscale porosity also offers multiscale biomimetic mechanical properties for better tissue integration, myogenesis, and functional muscle recovery [52,63]. A 15% GelMA solution was selected as the foam precursor to recapitulate the desired biomimetic mechanical properties. On a macroscale perspective, the elastic modulus of the foam is very close to that of bulk skeletal muscle (around 8 kPa for foam vs 8-17 kPa reported for skeletal muscle [52]). On a microscale view, the elastic modulus of the GelMA regions between the bubbles resembles the elastic modulus of individual muscle fibers (around 80 kPa for GelMA hydrogel vs 50 and 100 kPa for fast and slow-twitch fibers [53]).

In addition, foaming also enhanced the deformability of the scaffold. Since muscles contract, a highly deformable implant capable of complying with large strains is desirable [64]. The foam scaffold demonstrated close to 300% deformability in shear tests, making it an ideal candidate for skeletal muscle tissue engineering. Furthermore, the shear tests showed a strong adhesion of the scaffold to the muscle tissue. Secure adhesion of the implants to the tissue ensures minimum displacement of the implant during the surgery or as a result of body movement post surgery, enhancing the likelihood of implant-tissue integration [24]. GelMA hydrogel has been reported to establish strong adhesion to the tissue upon *in situ* crosslinking due to the physical interlocking,

the formation of covalent bonds upon generation of free radicals during photocrosslinking, and hydrogen bonds between free hydroxyl groups in the GelMA structure and the tissue [24,65,66]. Our results were in agreement with previous findings. However, GelMA foams were more flexible and therefore the adhesion strength of GelMA foam was comparable to the values of GelMA hydrogel.

IGF-1 was incorporated into the scaffold as it is decreased following VML injury and is an important myogenic factor, known to exert anabolic effects on muscle. Here, we demonstrated that IGF-1 could enhance the proliferation and differentiation rate of muscle progenitors. Previous reports demonstrated that increased myoblast density can promote their alignment [39], which is important for their differentiation and final muscle fiber functionality [46]. Better aligned organization was observed in the myoblasts cultured with a physiologically relevant IGF-1 level, in agreement with previous studies [8,67]. Further, previous IGF-1 optimization resulted in more mature myotube fusion at and above 10 ng/mL [41]. Importantly, localized, targeted application of IGF-1 has an important biological advantage in that it will mitigate any potential adverse effects of increasing the systemic level of IGF-1 and manipulating the GH-axis, such as hypoglycemia and reduced GH release [68,69]. Due to multifaceted functions of IGF-1 and different populations that should be targeted, a suitable scaffold should controlled release part of IGF-1 to affect cells within the remnant tissue and retain part of that to target cells that have grown into the scaffold. The encapsulation of IGF-1 into the foam scaffolds results in gradual release of the molecule over days. However, to sustain the release and retain IGF-1 in the scaffold, an auxiliary system was used. Since IGF-1 is positively charged [49] a strategy was developed to avoid its burst release from a positively charged GetMA foam network due to repulsive electrostatic interactions (GelMA is made from positively charged gelatin type A [48]). Negatively charged gelatin microparticles were used as the carrier of a positively charges molecule. Microparticles were first loaded with IGF-1 and then encapsulated into the foam structure.

The composite bioink was tested for its printability before implementing on a murine model for VML. When printing a gelatin-based material, partial thermal gelation is required before extrusion of the material through the nozzle to prevent under-gelation or over-gelation that causes poor printability [54]. However, controlling thermal gelation of GelMA and therefore its 3D printing is extremely challenging and the bioink often suffers from under-gelation or over-gelation [54]. In contrast, we found the foam bioink highly printable. This is due to its rapid sol-gel transition. Upon extrusion, the foam solution immediately solidifies as a result of thermal gelation, forming a

smooth filament at the nozzle tip as shown by our results, even if the bioink is at temperatures above sol-gel transition and therefore is completely in solution phase inside the syringe. More rapid sol-gel transition of foam compared to unmodified GelMA is due to the low density of the foam bioink, making its surface-area-to-volume ratio higher, accelerating the temperature change. It is noteworthy that an acellular bioink was developed in this study to provide an effective but simple and clinically translatable approach. While cellular scaffolds have been implemented widely in muscle tissue engineering, the application of the cells makes the process much more complex and the regulatory pathway toward clinical translation more cumbersome [1]. Furthermore, the testing of cellular scaffolds requires use of immunocompromised animals, which can skew the obtained results given the critical role of the immune system in muscle regeneration [8,70]. Additional benefit of acellular scaffolds over cellular scaffolds is faster response in the treatment of injury, which is critical in the clinical settings.

The developed strategy was tested for the treatment of acute VML injury in wild-type mice. To demonstrate the benefit of our IGF-1 impregnated foam scaffolds, we utilized a validated murine model of VML injury in which *en bloc* resection of the gastrocnemius muscle in the posterior compartment is performed [17,30,71]. This type of injury results in loss of both skeletal muscle strength and functional capacity, as measured by running endurance. Our results suggest that placement of an IGF-1 foam scaffold within an acute VML injury improves both skeletal muscle strength and functional recovery and, by eight weeks following injury, the functional status approaches healthy, uninjured muscle. In addition, this improvement in muscle function is accompanied by a decrease in fibrosis and evidence of *de novo* skeletal muscle regeneration within the scaffold itself. The recovery in muscle function demonstrated here is similar to others who have employed the use of cells [45].

Others have demonstrated improvements in VML recovery following scaffold placement, including VML treatment with porcine urinary bladder extracellular matrix [36] or collagen glycosaminoglycan matrixes [32]. Importantly, a recent meta-analysis suggested that functional strength improvement was only marginal with the use of acellular scaffold therapy (16%) in comparison with no treatment at all, which may be partially attributable to poor tissue ingrowth [72]. Separately, decellularized scaffolds, hydrogels, nanofibers, and electroconductive scaffolds have all been evaluated, with equivocal benefit [73]. The modest functional improvement provided correlates to mixed results on the ability of scaffolds to promote *de novo* skeletal muscle

regeneration [74]. Our previous studies suggest a small improvement in functional muscle recovery following VML with the use of GelMA or collagen GAG scaffolds, but with minimal tissue ingrowth within the scaffold itself [28,75]. The use of a foam scaffold, however, is distinct in the amount of tissue growth within the scaffold itself and limitation of fibrosis.

Physical therapy is an important part of rehabilitation following muscle injury [72]. Exercise-based therapies remain the most commonly prescribed, clinically proven methods for promoting functional recovery after muscle injuries and may impact muscle regeneration [17,72,76], although with limited efficacy. In order to better simulate the clinical setting and to test the effect of exercise on the foam-based treatment for VML recovery, VML treatment was followed by regimented exercise. VML treated with Foam + IGF scaffold demonstrated significantly higher *in situ* force production when it was also exercised, and the group additionally outperformed the VML only and Foam only groups in both the maximal running distance and force production, indicating a synergetic effect of those two treatments. The exact mechanism(s) by which exercise enhances the therapeutic effects of the IGF foam remains to be elucidated, but several or a combination of the following may describe plausible interplays between the two treatments. Activity-induced muscular adaptations rely mostly on local (as opposed to systemic) production of growth factors in response to mechanosensory stimulation of muscle contraction within skeletal muscle. Those factors in turn exert anabolic effects on the exercised muscle in a paracrine fashion [77,78]. Exercise has been shown to augment circulation, angiogenesis, and hasten (re-)innervation of muscles following injuries[10,79,80], and these likely facilitate faster functional recovery. Overall, combined rehabilitation and regeneration therapy with IGF-releasing scaffold seem to work synergistically, and the observed functional benefits demonstrate a promising prospect for its clinical application.

In conclusion, while a variety of tissue engineering strategies have been proposed in prior studies for implantation into the muscle defects with promise in limiting fibrosis and improving hypertrophy of remnant muscle[1,18], this study demonstrates that GelMA foam scaffolds, impregnated with IGF-1, can improve functional muscle recovery in an acellular fashion. This renders foam scaffolds a highly translatable therapy. The strategy used here is very simple, translatable, and effective, which can be attributed to the higher capability of cell infiltration and myogenesis inside the foam as a result of its higher porosities, a homogeneous and interconnected pore network, and sustained release of IGF-1.

The method proposed in this study is novel from different perspectives, which can provide new opportunities for future works: (i) The simple and translational but robust approach for inducting the porosity in engineering scaffolds, enhancing cellular activity and inflammatory signaling, can be used for regeneration of various tissue defects; (ii) the control over the release kinetics of the IGF-1 from a hydrogel scaffold using electrostatic interaction between the GelMA, growth factor, and gelatin microparticles can be used for various drug delivery applications; (iii) the colloidal bioinks with enhanced printability can be implemented for various tissue engineering applications; (iv) the combination of easy and rapid preparation of microengineered acellular scaffold and *in situ* printing can facilitate intraoperative regenerative medicine; and finally (v) the combination of *in situ* printing of the microengineered scaffolds and physical therapy for the treatment of VML can offer a promising treatment capable of implementation in clinical practices. However, before clinical translation, the strategy should be investigated and refined in different aspects. First, the strategy should be implemented in large animal models. A scaffold implanted in large defects may limit nutrient transport and cellular infiltration, even when mesoporous scaffolds are implemented, reducing the regeneration capability of the method. The simultaneous printing of sacrificial filaments can help nutrient and oxygen transport and therefore enhance vascularization and final tissue regeneration. Second, the regeneration state of the muscle should be studies in earlier and later time points to better decipher the mechanism behind the regeneration and long-term effects of the therapy. Finally, the strategy can implement the supplementation of muscle progenitors, for example derived from induced pluripotent stem cells, to accelerate the muscle regeneration. However, the latter may result in increased complexity and more strict regulatory pathways.

4 Materials and Methods

4.1 Materials

Recombinant Mouse IGF-1 was obtained from R&D Systems (MN, USA). Cell culture reagents including Dulbecco's phosphate-buffered saline (DPBS), Dulbecco's modified eagle medium (DMEM), fetal bovine serum (FBS), penicillin-streptomycin (PS), trypsin-ethylenediaminetetraacetic acid (trypsin-EDTA), hourse serum (HS) and 4-(2-hydroxyethyl)-1-piperazineethanesulfonic acid (HEPES) were purchased from Thermofisher Scientific (Gibco, MA, USA). For characterization of *in vitro* cell studies, PrestoBlue™ reagent (Invitrogen), Alexa Fluor 488 Phalloidin, and DAPI were obtained from Thermofisher Scientific, while Triton X-100 and bovine serum albumin (BSA) were purchased from Sigma-Aldrich (MO, USA). Real-time quantitative PCR (RT-qPCR) reagents including TRIzol (Invitrogen), and SuperScript III First-Strand Synthesis SuperMix (Invitrogen) were purchased from Thermofisher Scientific, while iTaq Universal SYBR Green Supermix was obtained from Bio-Rad (CA, USA).

GelMA with a medium degree of methacrylation was synthesized based on an established protocol. Gelatin from porcine skin, type A, with a 300 g Bloom (Sigma-Aldrich) was dissolved in DPBS at a 10% concentration under 240 rpm stirring at 50°C for 1 h. Methacrylic anhydride was then added dropwise to the solution at a 1.25% (v/v) concentration, followed by its incubation under vigorous stirring (500 rpm) for 1h. To stop the reaction, the solution was diluted with DPBS eight times and stirred at 240 rpm and 50°C for 10 min. The solution was then transferred into dialysis tubing with 12-14 kDa cutoff pore size (Spectrum, Fisher Scientific) and dialyzed against DI water for a week at 40°C by changing the water twice a day. Finally, the solution was filtered using Steritop vacuum filters (Sigma-Aldrich), frozen at -80°C for two days, and lyophilized for a week in a FreeZone® benchtop freeze dryer (Labconco®, MO, USA) to obtain dried GelMA. GelMA was stored at -20°C until use.

Gelatin microparticles were synthesized using a desolvation approach. A 5% (w/v) type B gelatin from bovine skin (225 g Bloom, Sigma-Aldrich) was prepared by stirring at 200 rpm and 50°C. Then, acetone (Sigma-Aldrich) was added to the solution at a 1:1 volumetric ratio at room temperature and the supernatant was discarded. The precipitate was redissolved in DI water to recover the volume of the solution and pH was adjusted to 12 by the addition of 3 mol/L NaOH (Sigma-Aldrich). Acetone was then added dropwise at a 3:1 volumetric ratio (acetone:gelatin solution), and the solution was shaken for 10 min, followed by the addition of glutaraldehyde (25%

solution, Sigma-Aldrich) at a 0.25% (v/v) concentration. The solution was stirred overnight at 50°C and 200 rpm and particles were harvested by triple centrifugation (10,000g for 30 min) and redispersion in a 100% ethanol solution. The particles were subsequently freeze-dried for 12 h and stored at -20°C until use.

4.2 Cell culture

C2C12 mouse myoblast cells were subcultured up to passage 10 by detaching the cells using Trypsin-EDTA and resuspending in a growth medium containing DMEM supplemented with 10% FBS and 1% PS. For the main experiments, the cells were cultured for 7 days in the growth media containing IGF-1 at 0 ng/ml, 1 ng/ml, or 10 ng/ml concentrations. After 7 days, the culture medium was replaced with a differentiation medium, composed of DMEM supplemented with 2% HS, 20 mM HEPES, and 1% PS. C2C12 cells were cultured in the differentiation medium containing 0 ng/ml, 1 ng/ml, or 10 ng/ml IGF-I for an additional 14 days of differentiation.

4.3 Evaluating the proliferation rate and morphology of the muscle progenitors

The cell proliferation rate and activity were determined during the culture time by incubating the cells in a solution composed of 10% (v/v) PrestoBlue™ reagent in the culture media. Cultures were placed in an incubator at 37°C and 5% CO_2 for 1.5 hours. 100 µL of the supernatant was then transferred to a 96 well plate. The fluorescence intensity was detected by a multimodal plate reader (BioTek Instruments Inc., VT, US) at an excitation wavelength of 560 nm and an emission of 590 nm.

Cellular morphology was assessed using F-Actin/DAPI staining. Samples were fixed by applying a 4% (w/v) paraformaldehyde solution for 30 min, followed by three washing steps with DPBS. The cells were then treated with 0.3% (v/v) Triton-X 100 in DPBS for 10 min and washed twice with DPBS. Samples were incubated in a 1% (w/v) BSA solution in DPBS for 30 min. Subsequently, Phalloidin with a dilution of 1:40 in DPBS was incubated with cells for 40 min at room temperature in dark. Cultures were washed again and then incubated in a 1:500 diluted DAPI solution in DPBS for 10 minutes. After a final washing step, cells were visualized under a fluorescence microscope (AxioCam MRc5, Carl Zeiss, Germany).

4.4 Assessment of myogenic differentiation using RT-qPCR

In order to investigate myoblast differentiation, the expression of relevant genes was measured by RT-qPCR. TRIzol was used to extract the RNA and NanoDrop (Thermofisher Scientific) was implemented to evaluate the total RNA yield. According to the manufacturer's instructions, 1 µg of the total RNA of each sample was reverse-transcribed by using the SuperScript III First-Strand Synthesis SuperMix. At this stage, RT-PCR was performed by introducing the SYBR Green Master Mix. A 20 µL volume reaction component was prepared by mixing 10 µL of Master Mix with 1 µL of forward and reverse primers and 100 ng of cDNA template, while nuclease-free water was used to adjust to the final volume. Relative gene expressions were calculated using a ΔΔCt method, through normalizing to GAPDH gene expression.

4.5 Bioink preparation

The bioink was consisted of 15% (w/v) GelMA, 1% (w/v) PVA, 1500 ng/ml IGF-1, 6 mg/ml gelatin microparticles, and 0.3% (w/v) lithium phenyl-2,4,6-trimethylbenzoylphosphinate (LAP, Sigma-Aldrich) as the photoinitiator. IGF-1 stock solution was prepared by reconstitution in DPBS containing 0.1% BSA. Gelatin microparticles were first loaded with IGF-1 by vortex mixing of 50 mg microparticles in 8000 ng/ml IGF-1 solution at 4°C overnight. 120 µL of the mixture was then added to 1 mL of GelMA solution, containing LAP and PVA, and vortex mixed for 20 sec to achieve the target concentrations.

To make the foam bioink, the biocomposite was added into a syringe barrel and foamed *in situ* by inserting the probe of a handheld homogenizer (Bio-Gen PRO200, ProScientific, CT, USA) inside the solution and stirring it for 40 sec at 15000 rpm. For crosslinking, a 1 watt 395 nm wavelength blue light was used either implementing the integrated LED into the handheld printer or an LED flashlight.

4.6 SEM analysis

SEM was performed to investigate the internal microstructure of the printed foam scaffolds. The bioink was printed on the glass slides and photo-crosslinked. The scaffolds were submerged into liquid nitrogen to immediately freeze the hydrogel and subsequently lyophilized for 24 h. The scaffolds were then broken to expose the cross-section and were coated with a thin gold layer using a sputter coater device (Vacuum Desk V, TX, USA) set at 60 sec and 20 mA. The samples were

imaged using a benchtop SEM device (TM-1000, HITACHI) and images were analyzed using ImageJ software. The average pore or particle sizes obtained from at least three different samples were considered as different replicates.

4.7 Assessment of release kinetics

The release of IGF-1 was evaluated from four groups: IGF-1 loaded into gelatin microparticles, IGF-1 loaded into gelatin microparticles and IGF-1 freely encapsulated in a bulk GelMA hydrogel, IGF-1 freely encapsulated into a foamed GelMA hydrogel, and IGF-1 loaded into gelatin microparticles and IGF-1 freely encapsulated into a foamed GelMA hydrogel. In the hydrogel groups with microparticles, 2/3 of the final IGF-1 concentration was bound to microparticles and 1/3 was freely encapsulated into the hydrogel. 100 µL of the foamed hydrogel or bulk hydrogel was printed into each well of a 48-well cell culture plate and crosslinked *in situ* as previously described (n = 4). The gelatin microparticle group that was not encapsulated in a scaffold was added into 100 µL of DPBS to account for the volume of the hydrogels in the other groups. 250 µL of DPBS solution (pH 7.2-7.3) was then added on top of the samples and the plate was sealed and incubated at 37°C. At each time point until day 14, 250 µL of the supernatant was removed and stored in a micro-centrifuge tube, and 250 µL of DPBS was added to each sample to replace the removed supernatant. The supernatants were stored at -20°C before measuring the IGF-1 concentration released at each time point. The IGF-1 concentrations were measured using a murine IGF-1 DuoSet ELISA kit (R&D Systems, MA, USA) based on the manufacturer's protocol.

4.8 Measurement of mechanical properties

Compression and lap shear tests were performed to evaluate the mechanical properties of the scaffolds in this work. An Instron 5542 mechanical tester (MA, USA) was used to perform the experiments. To perform the compression tests, the scaffolds were fabricated in cylindrical shape using a polydimethylsiloxane (PDMS; Dow, MI, USA) mold with 6 mm diameter and 5 mm height. To avoid overfilling, a glass slide was placed on top of the filled mold and the bioink was photocrosslinked through a glass slide as described before. The sample was then removed from the mold and placed between the compression plates of the device as shown in **Figure 3**. A compression rate of 1mm/min was then applied and the compression modulus was calculated from

the slope of a fitted line interpolating the stress-strain data up to 10% strain. The lap shear tests were performed based on ASTM F2255-05 standard [81]. Rectangular pieces of porcine muscle (13 mm × 10 mm) were cut and glued into glass slides using cyanoacrylate adhesive. The bioink was then printed onto the tissue with 13 mm × 10 mm × 2 mm dimensions, covered with 3-(trimethoxysilyl) propyl methacrylate (TMSPMA; Sigma-Aldrich) coated glass slide, and photocrosslinked as described. The samples were subsequently secured on the mechanical testing device using grips (**Figure 3**) and pulled in shear at a rate of 1 mm/min until failure occurred.

4.9 *Handheld printer and printing experiments*

The handheld printer was developed as previously described [24,28,29]. An extrusion system was custom designed to transmit rotation from an electric micromotor (Pololu) through a linear guide rail system utilizing rolling bearings and precision shafts to a syringe filled with the bioink. Electronic control systems were also designed to control the motor power, speed, and direction as well as to activate the photocrosslinking system. The photocrosslinking system utilized a 1 W Blue LED (395 nm, CH_Town Electronic). The system was powered by a 2500 mAh battery (GTF) that was charged from a PowerBoost 1000 Charger (Adafruit). A customized housing was designed using SolidWorks (Dassault Systèmes) to enclose all systems while minimizing the device footprint and maximizing ergonomics during operator printing. The housing was 3D printed using stereolithography in an Objet260 Connex3™ (Stratasys). All components were wired and assembled by hand. During the device operation, the syringe full of the bulk or foamed GelMA bioink was loaded into the device, extruded into the defect size at the appropriate flow rates through a conical 22 gauge nozzle [24], and crosslinked using the blue light.

4.10 *Animal studies*

4.11 *Animals*

All animal procedures were approved by the Institutional Animal Care and Use Committee of Brigham and Women's Hospital, and were performed in compliance with the U.S. National Institutes of Health guidelines. C57BL/6 mice (10-12 weeks of age) were obtained from Jackson Laboratories. Animals were housed at the Brigham and Women's Hospital Animal Care Facility and were given *ad libitum* access to food and water following a 12 light / 12 dark cycle. An equal number of male and female gender mice were utilized in experiments.

4.11.1 VML injuries

VML was created on the gastrocnemius muscle bilaterally as follows: Under general anesthesia, depilation of legs was performed using a clipper and razor. After sterilization with chlorhexidine wipe, a skin incision was made along the posterior compartment of the hindlimb followed by dissection of the fascia to fully expose the underlying gastrocnemius muscle. Using a 4mm biopsy punch, a full thinness muscle defect was created in the mid-section of the gastrocnemius muscle without separating the muscle. The defect was then filled completely with either bioprinting of the foam or foam + IGF or without any treatment. The skin and fascia incisions were then closed with simple sutures (4-0 Silk, Ethicon, Johnson, Somerville, NJ, USA). The sham group received the skin opening/closure without muscle injury. Animals were allowed to heal in their respectable cages, with the freedom to access food, and water and move around in the cage. After 8 weeks, animals were subjected to the muscle strength measurements (torque measurements and *in situ* force measurements, as described below), and euthanized to harvest the injured muscles for histological evaluation.

4.11.2 Torque measurements

Torque produced by the plantar flexor muscle of the lower limb was measured 8 weeks following the muscle injuries. Under general anesthesia, the animal's foot was secured to the footplate using adhesive tape. The tibia was aligned so that it is perpendicular to the lever. The muscle group is stimulated by placing the EMG electrodes subcutaneously to stimulate the sciatic nerve. Using the device program (610A Dynamic Muscle Control LabBook v6, Aurora Scientific, Aurora, Ontario, Canada), the current and resting tension were adjusted until maximum twitch force was produced by a single pulse with the pulse width of 0.2 ms. Torque is measured as the force measured during tetanus at this optimized setting, normalized to one of the body weights of the animals (g).

4.11.3 In situ force measurements

In situ force tests were performed 8 weeks following muscle injury. Under general anesthesia, the skin and fascia were incised to expose the right GA muscle. The Achilles tendon was then severed at its distal end and sutured onto the lever arm of the force transducer. The soleus muscle

was dissected from the tendon and removed. To stabilize the leg in position, a needle was inserted directly through the knee and the needle was then locked in place. The exposed muscle was kept moist using Ringer solution. The GA muscle was stimulated by needle electrodes placed directly on the corresponding by resting the electrodes directly on the muscle. Using the device program (610A Dynamic Muscle Control LabBook v6, Aurora Scientific, Aurora, Ontario, Canada), the current and resting tension were adjusted until maximum twitch force was produced by a single pulse with a pulse width of 0.2 ms. The optimal length (Lo) in which muscle could produce its largest force was measured as the distance between the knee and distal insertion of muscle to the tendon. Under the optimal resting tension, the tetanic force was measured with pulses given at 100 Hz with increasing amperage from 10mA to 1A. The maximum twitch and tetanic forces of the right GA muscle of each animal were normalized to the estimated cross-sectional area (CSA) of the muscle (mm2) calculated as CSA = Muscle weight (mg)/[1.06×Lo(mm)].

4.12 Exercise therapy

In order to evaluate the effects of exercise on the VML treatments, VML injuries were inflicted on the gastrocnemius muscles of mice bilaterally as previously described. The VML was subsequently treated with foam + IGF or no treatment. Following 3 days of recovery, the animals were acclimatized to running on a treadmill for 3 days, and then subjected to an 8-week-long running exercise regimen on the treadmill at 12 m/min for 40 minutes, three times weekly or no regimented exercise training program. They were allowed to move freely within their cages for the remainder of the time and were given free access to food and water. The animals were trained at the same time each time at 8 PM. At the end of 8 weeks, the maximal distance of running was measured. Briefly, the maximal distance of running was measured as the distance run by the animal at 15 m/s before it definitively stopped running, where it was assumed to be the point of exhaustion. 2 days following the physiological testing above, functional recovery of the muscle was tested through in situ measurement of GA muscle force, as described in the previous section.

4.13 Histological staining and quantifications

The cryostat muscle cross-sections were stained for Hematoxylin and Eosin (HE) and Masson trichrome (MT) using standard techniques. For immunostaining, briefly, frozen sections were thawed at room temperature for 10-20 minutes. The slides were washed twice in phosphate-

buffered saline (PBS) and then incubated for 5 min in 0.05% TX-100 in PBS for permeabilization. The slides were then washed again in PBS and incubated at room temperature for 1h in a blocking solution containing 1% BSA and 5% Goat normal serum in TBS, followed by overnight incubation at 4 °C with primary antibodies (supplementary table 1) diluted in blocking buffer. Samples were washed three times in PBS and then incubated for 1 h at room temperature with secondary antibodies (supplementary table 1). The slides were then washed twice with PBS and incubated in DAPI solution for nuclei staining for 5 min. After washing the slides several times with PBS, they were mounted with ProLong™ Diamond Antifade Mountant (Invitrogen™) and glass coverslips. Olympus model BX53 microscope (UCMAD3, T7, Japan) was used to capture histological images and ImageJ (version 1.52a; Media Cybernetics, Rockville, MD, USA) was used for image analysis and quantifications. Briefly, for collagen deposition (fibrosis) quantification, the color deconvolution and image thresholding plugins of ImageJ were used to analyze the blue area in five high power field photos (HPF) of MT-stained slides in the injury site of each muscle cross-section. To quantify embryonic myofibers, a number of eMHC positive myofibers were measured manually in three HPF images of the regenerating site of each muscle cross-section. Similarly, AchRs were quantify manually to measure the number of NMJs in the regenerating area of the muscle.

4.14 Statistical Analysis

All of the data were presented as mean ± standard deviation. The statistical analyses were performed using GraphPad Prism 9.0 software (CA, USA). One or two-way analyses of variance (ANOVA) were used in this work to compare the groups and p-values smaller than 0.05 were considered significant and shown in the graphs.

5   Acknowledgments

References

1   Samandari, M. *et al.* Bioinks and bioprinting strategies for skeletal muscle tissue engineering *Advanced Materials* (2022).

2   Rivas, D. A. & Fielding, R. A. in *Encyclopedia of Human Nutrition (Third Edition)* (ed Benjamin Caballero) 193-199 (Academic Press, 2013).

3   Hall, J. *Guyton and Hall Textbook of Medical Physiology*. 13th edn, (Elsevier, 2015).

4   Relaix, F. *et al.* Perspectives on skeletal muscle stem cells. *Nature Communications* **12**, 1-11 (2021).

5   Endo, Y. *et al.* Loss of ARNT in skeletal muscle limits muscle regeneration in aging. *The FASEB Journal* **34**, 16086-16104 (2020).

6   Järvinen, T. A. H., Järvinen, T. L. N., Kääriäinen, M., Kalimo, H. & Järvinen, M. Muscle Injuries: Biology and Treatment. *The American Journal of Sports Medicine* **33**, 745-764, doi:10.1177/0363546505274714 (2005).

7   Wang, Y. X. & Rudnicki, M. A. Satellite cells, the engines of muscle repair. *Nature Reviews Molecular Cell Biology* **13**, 127-133, doi:10.1038/nrm3265 (2012).

8   Tidball, J. G. Regulation of muscle growth and regeneration by the immune system. *Nature Reviews Immunology* **17**, 165-178, doi:10.1038/nri.2016.150 (2017).

9   Endo, Y., Nourmahnad, A. & Sinha, I. Optimizing skeletal muscle anabolic response to resistance training in aging. *Frontiers in physiology* **11**, 874 (2020).

10   Grogan, B. F. & Hsu, J. R. Volumetric muscle loss. *J Am Acad Orthop Surg* **19 Suppl 1**, S35-37, doi:10.5435/00124635-201102001-00007 (2011).

11   Corona, B. T., Rivera, J. C., Owens, J. G., Wenke, J. C. & Rathbone, C. R. Volumetric muscle loss leads to permanent disability following extremity trauma. *Journal of Rehabilitation Research & Development* **52** (2015).

12   Nuutila, K. *et al.* Gene expression profiling of skeletal muscle after volumetric muscle loss. *Wound Repair and Regeneration* **25**, 408-413, doi:https://doi.org/10.1111/wrr.12547 (2017).

13   Grasman, J. M., Zayas, M. J., Page, R. L. & Pins, G. D. Biomimetic scaffolds for regeneration of volumetric muscle loss in skeletal muscle injuries. *Acta Biomater* **25**, 2-15, doi:10.1016/j.actbio.2015.07.038 (2015).

14   Ulusal, A. E., Lin, C.-H., Lin, Y.-T., Ulusal, B. G. & Yazar, S. The use of free flaps in the management of type IIIB open calcaneal fractures. *Plastic and reconstructive surgery* **121**, 2010-2019 (2008).

15   Doi, K., Hattori, Y., Tan, S.-H. & Dhawan, V. Basic science behind functioning free muscle transplantation. *Clinics in plastic surgery* **29**, 483-495 (2002).

16   Lin, C.-H., Lin, Y.-T., Yeh, J.-T. & Chen, C.-T. Free functioning muscle transfer for lower extremity posttraumatic composite structure and functional defect. *Plastic and reconstructive surgery* **119**, 2118-2126 (2007).

17   Greising, S. M. *et al.* Early rehabilitation for volumetric muscle loss injury augments endogenous regenerative aspects of muscle strength and oxidative capacity. *BMC musculoskeletal disorders* **19**, 1-11 (2018).

18   Gilbert-Honick, J. & Grayson, W. Vascularized and innervated skeletal muscle tissue engineering. *Advanced Healthcare Materials* **9**, 1900626 (2020).

19   Costantini, M. *et al.* in *Biofabrication and 3D Tissue Modeling*   184-215 (2019).

20   Zhuang, P., An, J., Chua, C. K. & Tan, L. P. Bioprinting of 3D in vitro skeletal muscle models: A review. *Materials & Design* **193**, 108794, doi:https://doi.org/10.1016/j.matdes.2020.108794 (2020).

21   Ostrovidov, S. *et al.* 3D Bioprinting in Skeletal Muscle Tissue Engineering. *Small* **15**, 1805530, doi:10.1002/smll.201805530 (2019).

22   Murphy, S. V. & Atala, A. 3D bioprinting of tissues and organs. *Nature Biotechnology* **32**, 773-785, doi:10.1038/nbt.2958 (2014).

23   Samandari, M., Quint, J. & Tamayol, A. in *Musculoskeletal Tissue Engineering* (ed Yupeng Chen) 167-200 (Elsevier, 2022).

24   Nuutila, K. *et al.* In vivo printing of growth factor-eluting adhesive scaffolds improves wound healing. *Bioactive Materials*, doi:https://doi.org/10.1016/j.bioactmat.2021.06.030 (2022).

25   Singh, S., Choudhury, D., Yu, F., Mironov, V. & Naing, M. W. In situ bioprinting – Bioprinting from benchside to bedside? *Acta Biomaterialia* **101**, 14-25, doi:https://doi.org/10.1016/j.actbio.2019.08.045 (2020).

26   Albanna, M. *et al.* In Situ Bioprinting of Autologous Skin Cells Accelerates Wound Healing of Extensive Excisional Full-Thickness Wounds. *Scientific Reports* **9**, 1856, doi:10.1038/s41598-018-38366-w (2019).

27   Mostafavi, A. *et al.* In situ printing of scaffolds for reconstruction of bone defects. *Acta Biomaterialia* **127**, 313-326, doi:https://doi.org/10.1016/j.actbio.2021.03.009 (2021).

28   Quint, J. P. *et al.* In Vivo Printing of Nanoenabled Scaffolds for the Treatment of Skeletal Muscle Injuries. *Advanced Healthcare Materials* **n/a**, 2002152, doi:https://doi.org/10.1002/adhm.202002152 (2021).

29   Russell, C. S. *et al.* In Situ Printing of Adhesive Hydrogel Scaffolds for the Treatment of Skeletal Muscle Injuries. *ACS Applied Bio Materials* **3**, 1568-1579, doi:10.1021/acsabm.9b01176 (2020).

30   Mostafavi, A. *et al.* Colloidal multiscale porous adhesive (bio)inks facilitate scaffold integration. *Applied Physics Reviews* **8**, 041415, doi:10.1063/5.0062823 (2021).

31   Mulbauer, G. D. & Matthew, H. W. Biomimetic scaffolds in skeletal muscle regeneration. *Discoveries* **7** (2019).

32   Panayi, A. C. *et al.* A porous collagen-GAG scaffold promotes muscle regeneration following volumetric muscle loss injury. *Wound Repair and Regeneration* **28**, 61-74 (2020).

33   Verbeke, C. S. & Mooney, D. J. Injectable, Pore-Forming Hydrogels for In Vivo Enrichment of Immature Dendritic Cells. *Adv. Healthc. Mater.* **4**, 2677-2687, doi:10.1002/adhm.201500618 (2015).

34   Keskar, V., Marion, N. W., Mao, J. J. & Gemeinhart, R. A. In vitro evaluation of macroporous hydrogels to facilitate stem cell infiltration, growth, and mineralization. *Tissue Eng. Part A* **15**, 1695-1707, doi:10.1089/ten.tea.2008.0238 (2009).

35   Lieleg, O. & Ribbeck, K. Biological hydrogels as selective diffusion barriers. *Trends Cell Biol.* **21**, 543-551, doi:10.1016/j.tcb.2011.06.002 (2011).

36   Sicari, B. M. *et al.* An Acellular Biologic Scaffold Promotes Skeletal Muscle Formation in Mice and Humans with Volumetric Muscle Loss. *Science Translational Medicine* **6**, 234ra258-234ra258, doi:doi:10.1126/scitranslmed.3008085 (2014).

37   Xu, Y. *et al.* Melatonin-Based and Biomimetic Scaffold as Muscle–ECM Implant for Guiding Myogenic Differentiation of Volumetric Muscle Loss. *Advanced Functional Materials* **30**, 2002378, doi:https://doi.org/10.1002/adfm.202002378 (2020).

38   Kim, J. H. *et al.* Neural cell integration into 3D bioprinted skeletal muscle constructs accelerates restoration of muscle function. *Nature Communications* **11**, 1025, doi:10.1038/s41467-020-14930-9 (2020).

39   Kim, J. H. *et al.* 3D Bioprinted Human Skeletal Muscle Constructs for Muscle Function Restoration. *Scientific Reports* **8**, 12307, doi:10.1038/s41598-018-29968-5 (2018).

40   Karalaki, M., Fili, S., Philippou, A. & Koutsilieris, M. Muscle regeneration: cellular and molecular events. *In vivo* **23**, 779-796 (2009).

41   Quint, J. P. *et al.* Nanoengineered myogenic scaffolds for skeletal muscle tissue engineering. *Nanoscale* **14**, 797-814 (2022).

42   Ahmad, S. S., Ahmad, K., Lee, E. J., Lee, Y.-H. & Choi, I. Implications of Insulin-Like Growth Factor-1 in Skeletal Muscle and Various Diseases. *Cells* **9**, 1773, doi:10.3390/cells9081773 (2020).

43   Philippou, A. & Barton, E. R. Optimizing IGF-I for skeletal muscle therapeutics. *Growth Horm IGF Res* **24**, 157-163, doi:10.1016/j.ghir.2014.06.003 (2014).

44   Lee, K., Silva, E. A. & Mooney, D. J. Growth factor delivery-based tissue engineering: general approaches and a review of recent developments. *Journal of the Royal Society Interface* **8**, 153-170 (2011).

45   Quarta, M. *et al.* Bioengineered constructs combined with exercise enhance stem cell-mediated treatment of volumetric muscle loss. *Nature communications* **8**, 1-17 (2017).

46   Samandari, M. *et al.* Controlling cellular organization in bioprinting through designed 3D microcompartmentalization. *Applied Physics Reviews* **8**, 021404, doi:10.1063/5.0040732 (2021).

47   Naseer, S. M. *et al.* Surface acoustic waves induced micropatterning of cells in gelatin methacryloyl (GelMA) hydrogels. *Biofabrication* **9**, 015020, doi:10.1088/1758-5090/aa585e (2017).

48   Wang, H. *et al.* Oppositely Charged Gelatin Nanospheres as Building Blocks for Injectable and Biodegradable Gels. *Advanced Materials* **23**, H119-H124, doi:https://doi.org/10.1002/adma.201003908 (2011).

49   Mullen, L. M. *et al.* Binding and release characteristics of insulin-like growth factor-1 from a collagen–glycosaminoglycan scaffold. *Tissue Engineering Part C: Methods* **16**, 1439-1448 (2010).

50   Tomczak, K. K. *et al.* Expression profiling and identification of novel genes involved in myogenic differentiation. *The FASEB journal* **18**, 1-23 (2004).

51   Farzin, A., Etesami, S. A., Quint, J., Memic, A. & Tamayol, A. Magnetic Nanoparticles in Cancer Therapy and Diagnosis. *Advanced Healthcare Materials* **9**, 1901058, doi:https://doi.org/10.1002/adhm.201901058 (2020).

52   Engler, A. J., Sen, S., Sweeney, H. L. & Discher, D. E. Matrix Elasticity Directs Stem Cell Lineage Specification. *Cell* **126**, 677-689, doi:https://doi.org/10.1016/j.cell.2006.06.044 (2006).

53   Kammoun, M. *et al.* Development of a novel multiphysical approach for the characterization of mechanical properties of musculotendinous tissues. *Scientific Reports* **9**, 7733, doi:10.1038/s41598-019-44053-1 (2019).

54   Ouyang, L., Yao, R., Zhao, Y. & Sun, W. Effect of bioink properties on printability and cell viability for 3D bioplotting of embryonic stem cells. *Biofabrication* **8**, 035020, doi:10.1088/1758-5090/8/3/035020 (2016).

55   Yue, K. *et al.* Synthesis, properties, and biomedical applications of gelatin methacryloyl (GelMA) hydrogels. *Biomaterials* **73**, 254-271, doi:https://doi.org/10.1016/j.biomaterials.2015.08.045 (2015).

56   Rahimi Mamaghani, K., Morteza Naghib, S., Zahedi, A. & Mozafari, M. Synthesis and microstructural characterization of GelMa/PEGDA hybrid hydrogel containing graphene oxide for biomedical purposes. *Materials Today: Proceedings* **5**, 15635-15644, doi:https://doi.org/10.1016/j.matpr.2018.04.173 (2018).

57   Wilde, P., Mackie, A., Husband, F., Gunning, P. & Morris, V. Proteins and emulsifiers at liquid interfaces. *Advances in Colloid and Interface Science* **108-109**, 63-71, doi:https://doi.org/10.1016/j.cis.2003.10.011 (2004).

58   Eggermont, L. J., Rogers, Z. J., Colombani, T., Memic, A. & Bencherif, S. A. Injectable Cryogels for Biomedical Applications. *Trends in Biotechnology* **38**, 418-431, doi:https://doi.org/10.1016/j.tibtech.2019.09.008 (2020).

59   Huebsch, N. *et al.* Matrix elasticity of void-forming hydrogels controls transplanted-stem-cell-mediated bone formation. *Nat. Mater.* **14**, 1269-1277, doi:10.1038/nmat4407 (2015).

60   Griffin, D. R., Weaver, W. M., Scumpia, P. O., Di Carlo, D. & Segura, T. Accelerated wound healing by injectable microporous gel scaffolds assembled from annealed building blocks. *Nature Materials* **14**, 737-744, doi:10.1038/nmat4294 (2015).

61   Nih, L. R., Sideris, E., Carmichael, S. T. & Segura, T. Injection of Microporous Annealing Particle (MAP) Hydrogels in the Stroke Cavity Reduces Gliosis and Inflammation and Promotes NPC Migration to the Lesion. *Advanced Materials* **29**, 1606471, doi:10.1002/adma.201606471 (2017).

62   Han, L. *et al.* Mussel-inspired cryogels for promoting wound regeneration through photobiostimulation, modulating inflammatory responses and suppressing bacterial invasion. *Nanoscale* **11**, 15846-15861 (2019).

63   Engler , A. J. *et al.* Myotubes differentiate optimally on substrates with tissue-like stiffness : pathological implications for soft or stiff microenvironments. *Journal of Cell Biology* **166**, 877-887, doi:10.1083/jcb.200405004 (2004).

64   Lin, S., Liu, J., Liu, X. & Zhao, X. Muscle-like fatigue-resistant hydrogels by mechanical training. *Proceedings of the National Academy of Sciences* **116**, 10244-10249 (2019).

65   Shirzaei Sani, E. *et al.* Sutureless repair of corneal injuries using naturally derived bioadhesive hydrogels. *Science Advances* **5**, eaav1281, doi:10.1126/sciadv.aav1281 (2019).

66   Assmann, A. *et al.* A highly adhesive and naturally derived sealant. *Biomaterials* **140**, 115-127, doi:https://doi.org/10.1016/j.biomaterials.2017.06.004 (2017).

67   Yoshida, T. & Delafontaine, P. Mechanisms of IGF-1-mediated regulation of skeletal muscle hypertrophy and atrophy. *Cells* **9**, 1970 (2020).

68   Carroll, P. V. *et al.* Recombinant human insulin-like growth factor-I (rhIGF-I) therapy in adults with type 1 diabetes mellitus: effects on IGFs, IGF-binding proteins, glucose levels and insulin treatment. *Clinical Endocrinology* **49**, 739-746, doi:https://doi.org/10.1046/j.1365-2265.1998.00600.x (1998).

69   Jenkins, P. J. Growth hormone and exercise. *Clin Endocrinol (Oxf)* **50**, 683-689, doi:10.1046/j.1365-2265.1999.00784.x (1999).

70   Tidball, J. G. & Villalta, S. A. Regulatory interactions between muscle and the immune system during muscle regeneration. *American Journal of Physiology-Regulatory, Integrative and Comparative Physiology* **298**, R1173-R1187, doi:10.1152/ajpregu.00735.2009 (2010).

71   Dalske, K. A. *et al.* Independent of physical activity, volumetric muscle loss injury in a murine model impairs whole-body metabolism. *Plos one* **16**, e0253629 (2021).

72   Greising, S. M., Corona, B. T., McGann, C., Frankum, J. K. & Warren, G. L. Therapeutic approaches for volumetric muscle loss injury: a systematic review and meta-analysis. *Tissue Engineering Part B: Reviews* **25**, 510-525 (2019).

73   Langridge, B., Griffin, M. & Butler, P. E. Regenerative medicine for skeletal muscle loss: a review of current tissue engineering approaches. *Journal of Materials Science: Materials in Medicine* **32**, 1-16 (2021).

74   Greising, S. M. *et al.* Unwavering pathobiology of volumetric muscle loss injury. *Scientific reports* **7**, 1-14 (2017).

75   Panayi, A. C. *et al.* A porous collagen-GAG scaffold promotes muscle regeneration following volumetric muscle loss injury. *Wound Repair and Regeneration* **28**, 61-74, doi:10.1111/wrr.12768 (2020).

76   Aurora, A., Garg, K., Corona, B. T. & Walters, T. J. Physical rehabilitation improves muscle function following volumetric muscle loss injury. *BMC sports science, medicine and rehabilitation* **6**, 1-10 (2014).

77   Adams, G. R. Role of insulin-like growth factor-I in the regulation of skeletal muscle adaptation to increased loading. *Exercise and sport sciences reviews* **26**, 31-60 (1998).

78   Schwarz, A. J., Brasel, J., Hintz, R. L., Mohan, S. & Cooper, D. Acute effect of brief low-and high-intensity exercise on circulating insulin-like growth factor (IGF) I, II, and IGF-binding protein-3 and its proteolysis in young healthy men. *The Journal of Clinical Endocrinology & Metabolism* **81**, 3492-3497 (1996).

79   Garg, K. *et al.* Volumetric muscle loss: persistent functional deficits beyond frank loss of tissue. *Journal of Orthopaedic Research* **33**, 40-46 (2015).

80   Olfert, I. M., Baum, O., Hellsten, Y. & Egginton, S. Advances and challenges in skeletal muscle angiogenesis. *American journal of physiology-heart and circulatory physiology* **310**, H326-H336 (2016).

81   (ASTM Internatational, West Conshohocken, PA, 2003).

Supplementary Materials for:

Scaffolds with hierarchical porosity support tissue regeneration and exercise therapy-mediated functional recovery post volumetric muscle loss

Yori Endo[1,‡] , Mohamadmahdi Samandari[2,‡], Mehran Karvar[1,‡], Azadeh Mostafavi[3], Jacob Quint[2], Chiara Rinoldi[4,5], Iman K. Yazdi[4], Wojciech Swieszkowski[5], Joshua Mauney[6], Shailesh Agarwal[1], Ali Tamayol[2,3]*, Indranil Sinha[1,]*

[1]Division of Plastic Surgery, Brigham and Women's Hospital, Harvard Medical School, Boston, MA 02115, USA

[2]Department of Biomedical Engineering, University of Connecticut, Farmington, CT 06269, USA

[3]Department of Mechanical and Materials Engineering, University of Nebraska-Lincoln, Lincoln, NE 68588, USA

[4]Division of Engineering in Medicine, Brigham and Women's Hospital, Harvard Medical School, Boston, MA 02115, USA

[5]Materials Design Division, Faculty of Material Science and Engineering, Warsaw University of Technology. Warsaw 02-507, Poland

[6]Departments of Urology and Biomedical Engineering, University of California, Irvine, Irvine, CA 92868, USA

‡: Y. Endo, M. Samadari, and M. Karvar contributed equally to the manuscript.

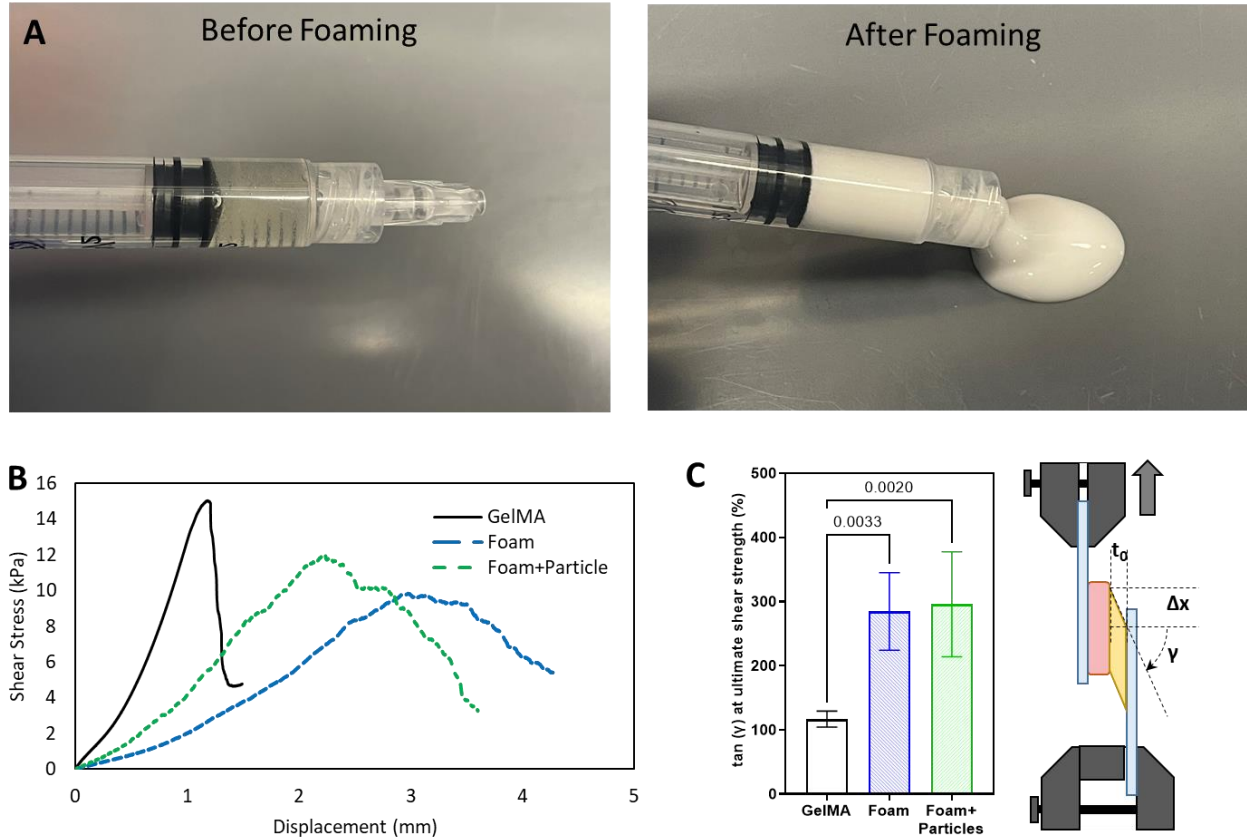*Corresponding authors: A. Tamayol: atamayol@uchc.edu; I. Sinha: isinha@bwh.harvard.edu

Figure S1. Appearance and Mechanical properties of the engineered scaffolds. (A) The appearance of the biomaterial before and after foaming. (B) Representative stress-strain curves of GelMA hydrogel, GelMA foam, and GelMA foam carrying gelatin microparticles. (C) Ultimate deformability of tested bioinks in lap shear test showing the resistance of the materials adhered to muscle tissue towards shear strain.
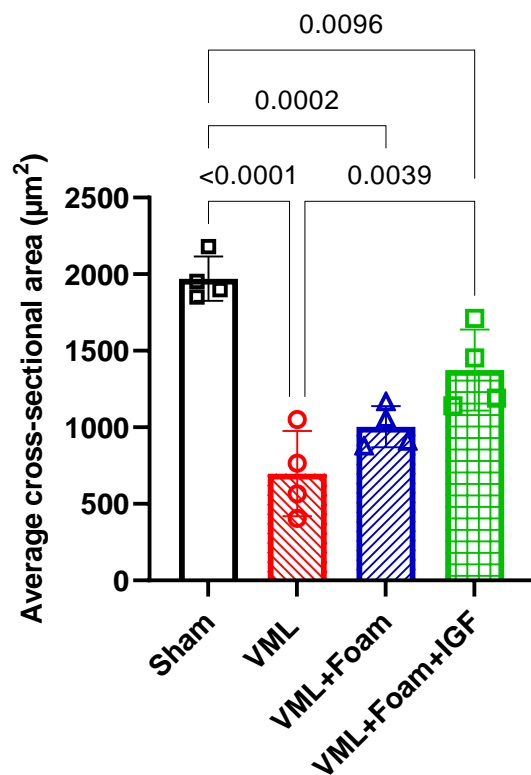
Figure S2. Average cross-sectional area (CSA) in μm² of multinucleated muscle fibers.

Table S1. List of the used antibodies

Antigen	Primary Antibody	Secondary Antibody
Laminin	Abcam, ab11575 Rabbit IgG 1:300 dilution	ThermoFisher, A-11012 Goat anti-Rabbit IgG H&L Alexa Fluor 594 1:400 dilution
MF20	NOVUS BIOLOGICAL, MAB4470 Mouse IgG2b 1:100 dilution	ThermoFisher, A-21140 Goat Anti-Mouse IgG2b Alexa Fluor 350 1:400 dilution
eMHC	DSHB F1.652 Mouse IgG1 5 ug/ml	ThermoFisher, A-21121 Goat Anti-Mouse IgG1 Alexa Fluor 488 1:400 dilution
AchR	Invitrogen™, B13422 (α-Bungarotoxin, Alexa Fluor™ 488 conjugate)	N/A